Journal of Metamorphic Geology

WILEY

Journal of METAMORPHIC GEOLOGY

ORIGINAL ARTICLE OPEN ACCESS

Fluid or Melt? Distinguishing Syn-Deformational Interaction Pathways

Hindol Ghatak[1] | Nathan R. Daczko[1] | Sandra Piazolo[2] | Tom Raimondo[3]

[1]School of Natural Sciences, Macquarie University, Sydney, New South Wales, Australia | [2]School of Earth and Environment, University of Leeds, Leeds, UK | [3]School of Natural and Built Environments, University of South Australia, Adelaide, South Australia, Australia

Correspondence: Nathan R. Daczko (nathan.daczko@mq.edu.au)

Received: 18 February 2025 | **Revised:** 20 June 2025 | **Accepted:** 30 July 2025

Funding: This work was supported by Australian Research Council (DP160103449).

Keywords: aqueous fluid | fluid–rock interaction | melferite | melt–rock interaction | mylonite | silicate melt

ABSTRACT

Understanding whether deformation occurred in the presence of aqueous fluid or silicate melt is crucial for interpreting ductile shear zones, impacting their thermal and geochemical evolution, and having rheological consequences. To identify the syn-deformational fluid type, we investigate contrasting shear zones active during the Alice Springs Orogeny in central Australia, focusing on their effects on dry granulite facies gneisses transformed into greenschist–amphibolite facies schists. Shear zones in the north-western part of the orogen (Reynolds–Anmatjira Ranges) exhibit greenschist–lower amphibolite facies muscovite–chlorite assemblages, quartz veins and microstructures indicative of solid-state deformation. These features collectively suggest deformation in the presence of aqueous fluid. In contrast, shear zones in the south-eastern part (Strangways Range) display upper amphibolite facies garnet–biotite–sillimanite assemblages, along with granitic dykes and lenses retaining igneous textures. Microstructures, such as 'string of bead' textures and felsic minerals forming films along grain boundaries or exhibiting low apparent dihedral angles, indicate the former presence of melt in high strain rocks. This suggests that hydration in the south-eastern shear zones was driven by externally sourced silicate melt and melt–rock reactions. Differentiating between the two types of shear zones using whole rock major and trace element data is challenging. However, rare earth element (REE) analyses show potential. Limited REE metasomatism is observed where aqueous fluids are inferred, with three samples in a transect displaying consistent patterns. In contrast, where silicate melt is interpreted as the metasomatic agent, REE metasomatism is more variable, exhibiting atypical REE patterns relative to common rock types and considerable variability between samples in a transect. This contrast is attributed to greater mobility of REEs in silicate melt compared to aqueous fluid.

1 | Introduction

Fluids play a pivotal role in mass and heat transfer within the Earth's crust, with aqueous fluids and silicate melts serving as primary agents (Yardley and Bodnar 2014; Tommasi et al. 2017). The efficiency of mass and heat transfer varies, generally being lower for aqueous fluids compared to silicate melts (Tommasi et al. 2017), subject to diverse physio-chemical parameters (Adam et al. 2014; Candela and Holland 1983). Many ductile shear zones, formed at different crustal levels, exhibit significant metasomatism, indicating their role as efficient conduits for fluid migration and contributors to mass transfer and rheological changes (Jefferies et al. 2006; Losh 1989; Mohanty and Ramsay 1994; Rutter and Neumann 1995).

Identification of high-strain zones relies on structural modifications, mineral assemblage changes and chemical alterations (Ramsay et al. 1983). Elemental mobility within shear zones

varies with fluid type, crucial for mineral systems science (Ague 2017; Hedenquist and Lowenstern 1994; Yardley and Bodnar 2014; Yardley 2009). In addition to economic considerations, studying fluids provides insights into thermal patterns during deformation, making it vital to distinguish between the former presence of aqueous fluid and silicate melt in shear zones.

Granulite terranes, due to their history of high-grade metamorphism and melt extraction, typically exhibit anhydrous and refractory mineral assemblages (Buick et al. 2008; Clarke et al. 2007). During tectonic activity, syn-deformational fluid-flow may lead to hydration, resulting in metasomatic changes, impacting various geological processes (Newton 1990). The nature of interacting fluids can range from CO_2-rich fluids to aqueous brines and silicate melts (Touret and Huizenga 2011), influencing crustal fracturing, stress distribution, partial melting and rheological behaviour (Iyer et al. 2008; Finch et al. 2016; Daczko et al. 2016). Such processes are linked to the initiation and evolution of orogenic systems, as seen in the Alice Springs Orogeny, where fluid ingress into shear zones led to crustal weakening (Raimondo et al. 2014; Piazolo et al. 2020).

The Alice Springs Orogen (Figure 1) provides an ideal setting for studying the former presence of aqueous fluid versus silicate melt in shear zones due to its exposure of different crustal levels of similar granulite facies basement that experienced deformation. Moving along a NW–SE transect from shallow to deeper crustal depths, shear zones exhibit significant variations; potentially reflecting differences in syn-deformational fluid types.

Previous studies on hydrous shear zones in the Reynolds–Anmatjira Ranges (Figure 1b,d,e) suggested fluxing by meteoric aqueous fluid based on low $\delta^{18}O$ and δD values (Raimondo et al. 2011). In contrast, shear zones in the Strangways Range (Figure 1b,c,f,g), inferred to have evolved under hotter and deeper conditions, show evidence of melt–rock interaction and metasomatism (Balle'vre et al. 2000; Bendall 2000; Piazolo et al. 2020; Daczko and Piazolo 2022; Silva et al. 2022; Ghatak et al. 2022). This research microstructurally and geochemically compares two subsolidus hydrated shear zones in the Reynolds–Anmatjira Ranges with two shear zones from the Strangways Range (Figure 1b), where interaction with migrating silicate melts caused the observed hydration in the deepest exposed levels of the orogen. The objective is to develop diagnostic criteria, based on these well-characterised case studies, that can be applied to other settings where the nature of the metasomatic fluid is less readily discernible.

1.1 | Background

Fluids play a crucial role in metamorphism and deformation by influencing reactions and rheology. These reactions can lead to either 'reaction strengthening' by the growth of cordierite, K-feldspar, andalusite, and garnet, or 'reaction weakening' by the replacement of rheologically hard minerals with phyllosilicates, or with grain size reduction (Wintsch and Dunning 1985; Vernon and Johnson 2000). During retrograde metamorphism, fluid access occurs via microfractures and/or high-strain zones (Yardley et al. 2000) with small proportions of fluid capable of driving substantial local metasomatism and hydration (Milke et al. 2013; Stenvall et al. 2020). While aqueous fluids are commonly implicated in retrogression, hydration may also result from the infiltration of water-rich silicate melts under prograde conditions (Stuart et al. 2017).

1.1.1 | Subsolidus Deformation

Subsolidus ductile shear zones exhibit microstructures such as undulose extinction, dynamic recrystallisation, shear band cleavages (Gapais and White 1982), mantled porphyroclasts (Passchier and Simpson 1986; Vernon 2000), mica fish (Lister and Snoke 1984) and myrmekite textures (Passchier and Trouw 2005). These features are influenced by strain and crustal depth. Fluid–rock interaction in these zones commonly involves dissolution–precipitation (e.g., Glassley et al. 2016) and depends on fluid composition (H_2O, CO_2 and brines). Despite lower fluid volumes at depth, fluid infiltration within shear zones may be self-propagating and involve significant volume loss (Essaifi et al. 2004). In granitic terrains, reactions such as the replacement of K-feldspar by muscovite depend on fluid composition (Yardley 2005). Garnet zoning in such environments can reflect evolving fluid chemistry (Raimondo et al. 2012).

1.1.2 | Deformation in the Presence of Melt

Deformation facilitates melt migration, where the presence of melt not only induces reactions but also profoundly influences rheology (Holyoke and Tullis 2006; Van der Molen and Paterson 1979; Stuart, Piazolo, and Daczko 2018; Piazolo et al. 2020). This can localise strain (Gardner et al. 2017), directing melt migration through percolative flow (Brown and Solar 1998) and shear-hosted dyking. High strain zones, with locally increased porosity and permeability, act as channels of lower fluid pressure, facilitating melt ascent through the crust (Etheridge et al. 2021).

Leucosomes in outcrop and microstructural features indicative of formerly melt-bearing rocks, recognised in experiments (Mehnert et al. 1973), include rounded minerals included in melt (Busch 1974), low dihedral angles, coeval crystallisation of quartz, K-feldspar and sodic plagioclase, and their occurrence in veinlets (Sawyer 1999; Vernon 2011; Bouchez et al. 1992). Additional criteria suggesting the former presence of melt encompass euhedral crystal faces of feldspar grains, or peritectic minerals like garnet, orthopyroxene or cordierite. Inclusion-free overgrowths, simple twinning in K-feldspar, aligned euhedral feldspar minerals, plagioclase with oscillatory zoning and biotite pseudomorphed by feldspar are also indicative (Holness and Clemens 1999; Clemens and Holness 2000). Symplectite reaction coronas with uniform mineral REE chemistry may also signal melt–rock interaction (Stuart et al. 2016, 2017; Gardner et al. 2025). Grain size criteria remain ambiguous (Sawyer and Brown 2008; Hasalova et al. 2008).

1.2 | Chemical Signatures of Metasomatism

Fluids are key agents of open-system metasomatism, driving mineral replacement and compositional change through

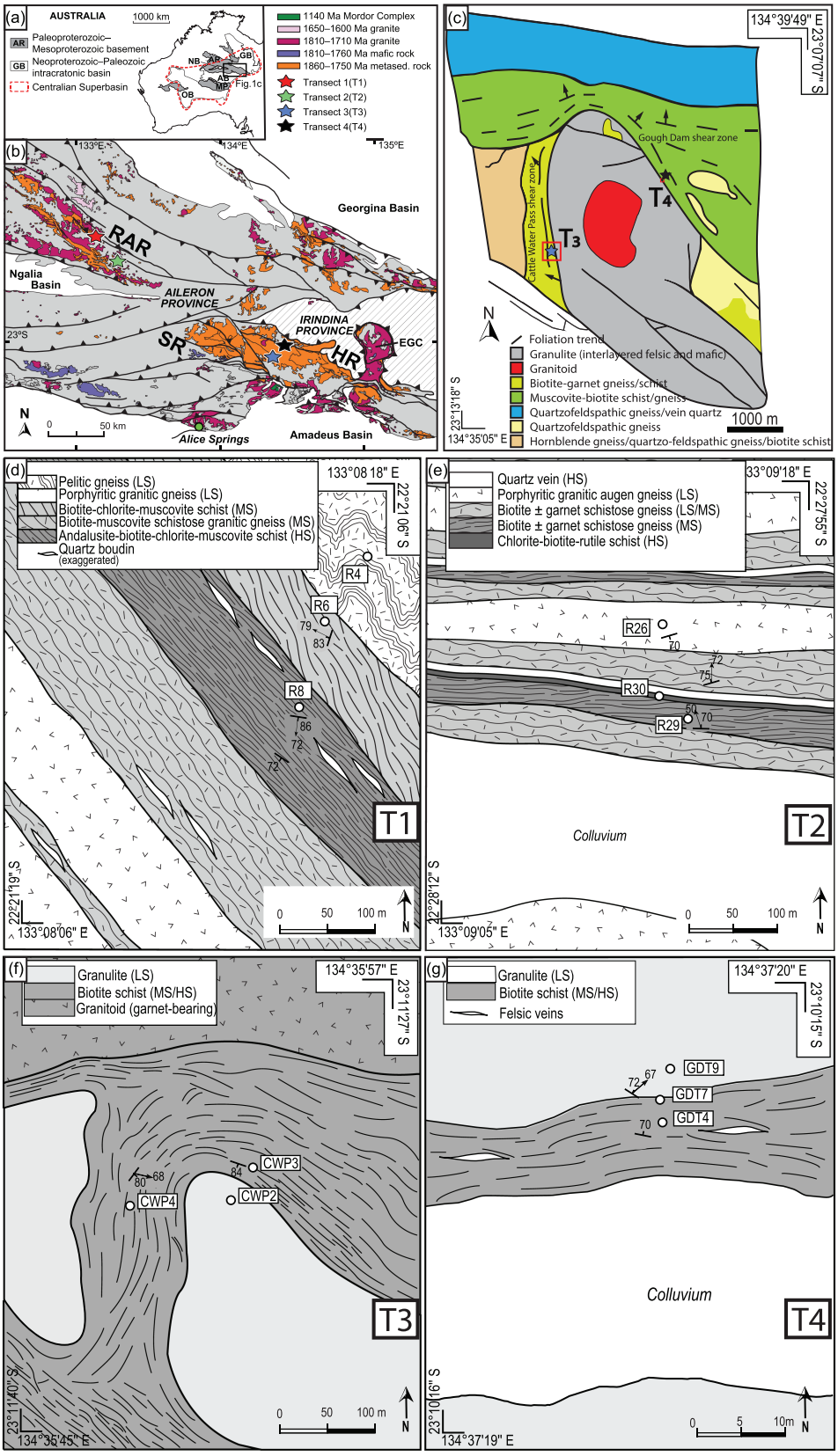

FIGURE 1 | Legend on next page.

diffusion and infiltration. Increasing variance is characteristic of metasomatic processes (Yardley 2009), where chemical components are nearly perfectly mobile in fluid, replicating conditions at their source (Korzhinskiĭ 1959). Fluid composition (H_2O, CO_2, brines, silicate melt) affects element mobility, with melt more effective at transporting incompatible and trace elements (Adam et al. 2014). Recent geochemical and experimental studies on melt–rock interactions (Beard et al. 2004; Daczko

FIGURE 1 | (a) The relative position of the Arunta region (AR) within Australia. (b) Regional geological map of the Arunta region showing the major tectonic subdivisions and the location of four shear zone transects examined in this study (T1–T4). Transects 1 and 2 across two shear zones are shown in the northwest in the Reynolds–Anmatjira Ranges (RAR). Transects 3 and 4 across two other shear zones are shown to the southwest in the Strangways Range (SR). All the coloured units form part of the Aileron Province. (c) A geological map of Mount Schaber region showing the Cattle Water Pass and Gough Dam shear zones. (d) Detailed outcrop map of T1 in the southeastern Anmatjira Range. (e) Detailed outcrop map of T2 in the Yaningidjara Hills, central Reynolds Range. (f) Detailed outcrop map of T3, Cattle Water Pass shear zone. (g) Detailed outcrop map of T4, Gough Dam shear zone.

et al. 2016; Stuart, Meek, et al. 2018; Meek et al. 2019; Gardner et al. 2025) indicate that migrating melt can induce substantial chemical changes. While aqueous fluids readily mobilise Na, Ca, K, Mg and Si, they are less efficient at transporting Fe, Al and REEs (Middelburg et al. 1988).

REE mobility serves as a proxy for fluid type, with higher solubility in silicate melts than aqueous fluids, except under extremely high pressure (Wendlandt and Harrison 1979). Minerals like monazite, apatite, epidote group minerals, garnet and xenotime control REE distribution; mobility is enhanced in halogen-, carbonate- or sulfate-rich fluids (Ague 2017). Melt-related metasomatism can cause profound chemical modification of host rock, while aqueous fluids typically yield more limited alteration.

2 | Geological Background

The Arunta Region, a 200,000 km^2 inlier of poly-deformed Proterozoic basement, encompasses amphibolite to granulite facies metamorphic rocks and less deformed granite (Figure 1a,b). Within this region, the Aileron Province constitutes a significant subdivision, documenting ancient tectonic events (> 1 Ga) marked by high geothermal gradient metamorphism, extensive felsic and mafic magmatism, and basin development (Hand and Buick 2001; Scrimgeour and Ahmad 2013). The last major tectonic event in the Arunta Region, the Palaeozoic Alice Springs Orogeny (ASO; 450–300 Ma), was intraplate, involving N–S contraction and resulting in the exhumation of mid to deep crustal rocks with anastomosing shear zones (Figure 1a,b; Cartwright et al. 1999; Raimondo et al. 2011).

The Alice Springs Orogen consists of the mid-crustal Reynolds–Anmatjira Ranges ('RAR') at the northeast (NE), the mid to deep crustal Strangways Range ('SR'), and the deep crustal Harts Range ('HR') at the southeast (SE) extremity of the Arunta Region (Figure 1b). The Reynolds–Anmatjira Ranges represent part of a crustal-scale pop-up structure exhuming mid-crustal granulites (Collins and Teyssier 1989). ASO-aged shear zones in this region, characterised by metasomatised features, trend NW–SE and deform Proterozoic folds and metamorphic fabrics (Collins and Teyssier 1989; Raimondo et al. 2011). P–T estimates for ASO shear zones here range from 400°C to 550°C and from 3.0 to 6.5 kbar (Hand and Buick 2001; Raimondo et al. 2012).

The Strangways Range to the southeast (Figure 1b) includes granulite facies rocks of the Strangways Metamorphic Complex, bounded by crustal-scale shear zones reactivated during the ASO. These shear zones form steeply dipping amphibolite- to greenschist-facies schist belts with S-directed thrusting. P–T estimates for ASO-aged shear zones in this region are ~600°C–660°C and 6–7 kbar. The Cattle Water Pass and Gough Dam shear zones are consistent with deformation in the presence of melt (Figure 1c; Piazolo et al. 2020; Ghatak et al. 2022; Silva et al. 2022).

The Harts Range primarily comprises metabasic and amphibolite–granulite facies metasedimentary rocks deposited in the Irindina subbasin, metamorphosed during the extensional Larapinta Rift event (~480–460 Ma) preceding the ASO. The Harts Range Group, reaching conditions of ~880°C and 10.5 kbar, controlled structural geometry during the ASO, showcasing its rheological influence (Tucker et al. 2015; Silva et al. 2018). Melt-present deformation is documented (Asimus et al. 2023) during the formation of the Entia Dome that forms an inlier of basement within the Irindina subbasin rocks.

3 | Methods and Analytical Techniques

3.1 | Petrography

Petrographic analysis employed polished thin sections of the samples, examined under optical microscopy utilising both plane and crossed polarised light at Macquarie University, Sydney, Australia. Additionally, the virtual petrographic microscope developed by Tetley and Daczko (2014) contributed to mineral identification and microstructure analysis, and all high-resolution photomicrographs can be viewed online in ImageMatrix (https://imagematrix.science.mq.edu.au/gallery/, search for 'RAN08'). Back-scatter electron (BSE) imaging was conducted on a Hitachi desktop scanning electron microscope (SEM) at the OptoFab node of the Australian National Fabrication Facility, Macquarie University. The SEM operated in low vacuum mode with an accelerating voltage of 15 kV. Mineral abbreviations are per Whitney and Evans (2010). The petrographic descriptions in the results section focus on the observed changes in mineral assemblage and microstructure, comparing three samples in a transect across shear zones, with the key feature being coupled progressive hydration with increasing strain.

3.2 | X-Ray Mapping

Micro XRF maps were generated using a Bruker M4 Tornado equipped with a Rh X-ray tube and dual Bruker x-flash EDS detectors. The analysis was performed at 50 kV and 200 μA, employing a 25 μm spot size and a 60 μm step. Data processing was executed using the Bruker M4 Esprit software package.

3.3 | Whole Rock Chemistry

Whole-rock geochemical analyses were conducted on carefully sampled 3–5 kg rocks from each location to highlight the modified rocks' heterogeneity compared to the large-scale homogeneity of host rocks. In the case of Reynolds–Anmatjira Ranges samples, fresh rock samples were crushed and homogenised using a tungsten carbide mill. For Strangways Range samples, rocks were crushed using a hydraulic press and then finely powdered (< 50 μm grain size) using an agate mill. Rigorous cleaning of the mill with Milli-Q water and ethanol between samples prevented cross-contamination.

Major element analysis took place at the Mark Wainwright Analytical Centre (UNSW), where 40 mm glass beads were prepared and analysed on a PANAlytical PW2400 WDXRF Spectrometer. Whole-rock trace element analyses were performed at Macquarie University using laser-ablation analysis of fused glass discs with an Agilent 7700cx quadrupole ICPMS attached to a Photon Machines Excite 193 nm excimer laser ablation system. Calibration standards included NIST 610 glass, and Ca served as the internal standard for quantifying trace element compositions. The raw data were processed using the GLITTER software package (Version 4.4; Griffin et al. 2008). Reference values for calibration were obtained from XRF standards, including AGV-2, BCR-2, BHVO-2 and GSP-2 (Table S1), and error margins in the analysed samples are detailed in Table S2.

4 | Field Relationships and Sample Petrography

The sampling locations are situated within granulite terrains intersected by hydrated shear zones. Our objective is to investigate the transformation of Proterozoic granulite into Palaeozoic mica schist during the Alice Springs Orogeny (ASO) (Norman 1991; Raimondo et al. 2011; Piazolo et al. 2020; Ghatak et al. 2022; Silva et al. 2022). To achieve this, samples representing various degrees of modification of the protolith were meticulously collected along four transects (T1–T4), with two in each of the Reynolds–Anmatjira and Strangways ranges.

Each transect was strategically chosen following extensive field mapping and thoughtful consideration of available options. Three samples were collected on each transect: one representing the least modified precursor homogeneous granulite, denoted as low strain (LS), characterised by low foliation intensity and located outside or adjacent to the shear zone. The other two samples within a transect showcased significantly modified granulite with intermediate to high foliation intensity, categorised as medium strain (MS) and high strain (HS), respectively. The classification into MS and HS was determined through (i) field assessment of strain-induced fabric development and sample location within the shear zone, (ii) petrographic evaluation of the mode of relict granulite mineral grains and (iii) examination of hydration degree based on new hydrous mineral formation.

The term 'strain' in LS, MS and HS loosely represents the extent of strain-induced fabric development, intricately linked with deformation, shearing and modification of relict mineral assemblages at an outcrop scale. In some instances, particularly in T1, the distinction between MS and HS was somewhat arbitrary, particularly when both samples from within the shear zone exhibited a very low mode of relict granulite mineral grains. Ensuring the collection of three samples from a single protolith was prioritised by selecting mapping areas where the precursor granulite exhibited homogeneity over tens to hundreds of meters outside the shear zone. Fully characterising heterogeneity within the shear zones, particularly for geochemical trends, would require many more MS and HS samples than examined in this study.

Transect locations are depicted in Figure 1b, and the transects are denoted as T1/T2 (Reynolds–Anmatjira Ranges) and T3/T4 (Strangways Range) (marked with red, green, blue and black stars, respectively, in Figure 1b).

All four shear zones selected for this study cut and hydrate granulite facies rocks within the Aileron Province of the Proterozoic Arunta region (Raimondo et al. 2011; Norman 1991). Two unnamed shear zones, 250 m and 150 m wide, from the Anmatjira and Reynolds Ranges were previously described by Raimondo et al. (2011), who concluded that both experienced an influx of meteoric aqueous fluid (Figure 1d,e). The remaining two shear zones are located in the Strangways Range (Cattle Water Pass and Gough Dam shear zones), each having a high-strain zone width of up to 400 m (Figure 1f,g; Norman 1991; Balle'vre et al. 2000). The regional metamorphic grade of the shear zones increases from NW to SE (i.e., from the Reynolds–Anmatjira Ranges to the Strangways Range), and Piazolo et al. (2020), Ghatak et al. (2022) and Silva et al. (2022) concluded that the Cattle Water Pass and Gough Dam shear zones involved melt-present deformation during the influx of an externally derived hydrous silicate melt, forming melferite zones (Daczko & Piazolo, 2022).

Key field relationships and sampling locations for each transect are illustrated in Figures 1 and 2, while thin section photomicrographs are presented in Figures 3 and 4, providing visual context for the progressive petrological changes associated with increasing strain and hydration. Comprehensive properties of the 12 selected samples are also outlined in Table 1 and Figure S1, presented as supporting information to offer an overview of the mineral modal differences among all samples.

4.1 | Anmatjira Range, Unnamed Shear Zone North of Sandy Creek Bore (Transect 1, T1)

A prominent 400 m wide shear zone, steeply dipping towards the northeast, is marked by kyanite- and andalusite-bearing biotite schists (Figure 1d, and indicated by the white dashed line on Figure 2a). This shear zone juxtaposes granitic orthogneiss (Anmatjira Orthogneiss, lighter orange rock, Figure 2a) and quartz–cordierite–biotite–sillimanite paragneiss (Weldon Metamorphics, darker brown rock, Figure 2a). The shear zone exhibits a NE/SW-plunging mineral elongation lineation defined by aligned mica, while S–C fabrics imply a reverse sense of movement (top to the SW). As the three samples in this transect are paragneisses, similar initial pelitic bulk compositions are inferred from the observation of aluminosilicate polymorphs in each sample. We sampled one kyanite-bearing and one andalusite-bearing schist from within the shear zone to compare

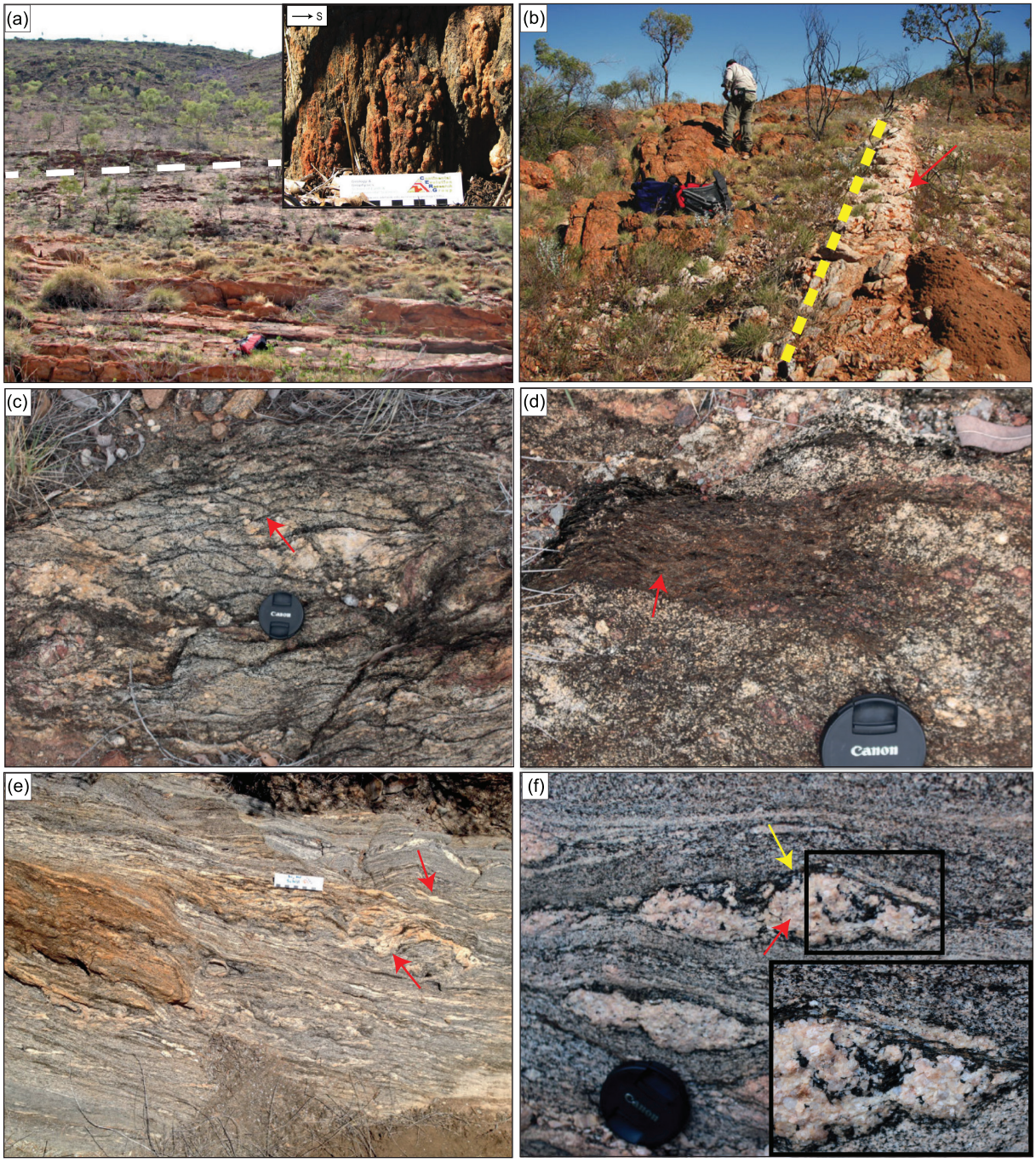

FIGURE 2 | (a) The boundary between the darker (brown) Weldon Metamorphics to the north and the lighter (orange) Anmatjira Orthogneiss to the south, Anmatjira Range is marked by a white dashed line (facing north) and inset shows steeply dipping andalusite-bearing shear zone. (b) Approximately 5 m wide deformed quartz vein (red arrow) subparallel to strike to shear fabric (yellow dashed line) from T2, Reynolds Range (facing east). (c) Anastomosing biotite-rich bands (red arrow) associated with felsic leucosomes within the Cattle Water Pass shear zone (T3), Strangways Range (plan view). (d) Biotite–garnet rich assemblage from the high strain domain within the Cattle Water Pass shear zone (T3), Strangways Range (plan view). (e) Foliation-parallel felsic veins (red arrows) within Gough Dam shear zone, Strangways Range (facing north). (f) Foliation-parallel granitic lenses (red arrow) within the Gough Dam shear zone shows euhedral grains and biotite selvedges (yellow arrow), Strangways Range (plan view).

to the sillimanite-bearing sample from outside the shear zone. Although the distinction between MS and HS is somewhat arbitrary along this transect, we refer to the kyanite-bearing schist as MS due to its location at the margin of the shear zone and the andalusite-bearing schist as HS based on its position near the centre of the shear zone.

Examining the paragneiss on the NE side of the shear zone (Figure 1d), the low-strain metapelitic sample outside the shear zone (sample R4-T1-LS) displays perthitic K-feldspar (0.5–0.7 mm), cordierite (0.5–1 mm), quartz (< 1 mm) and biotite (< 0.5 mm), with minor fine-grained sillimanite at grain boundaries (Table 1, Figures S1, 3a and 5a) and trace opaque minerals.

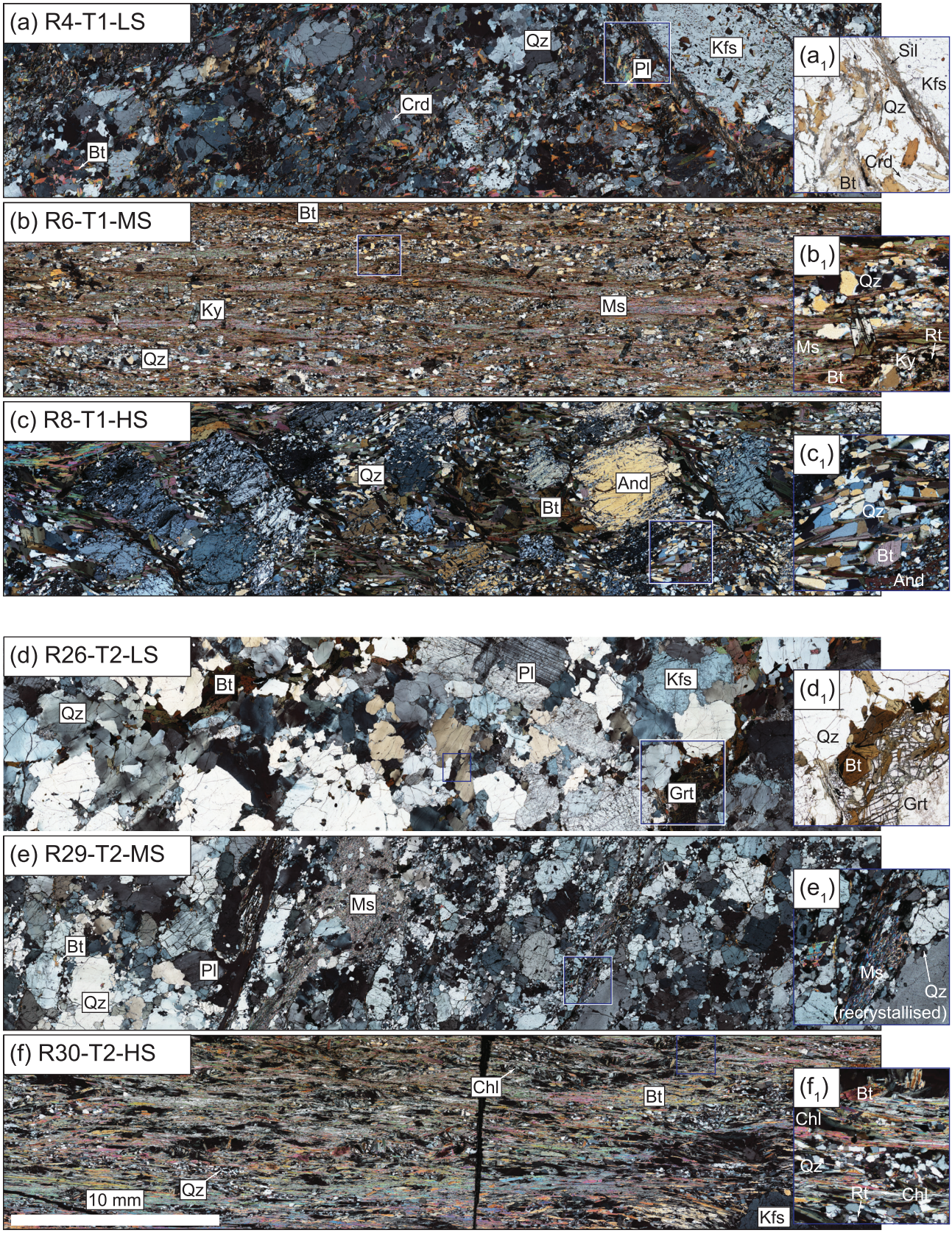

FIGURE 3 | Crossed polarised light (XPL) photomicrograph overview images of the entire length of the thin sections of the 6 samples (transects 1 and 2) from the Reynolds–Anmatjira Ranges. R = RAN008 (abbreviated sample prefixes of Raimondo et al. 2011). Transects 1 and 2 are denoted as T1 and T2 while LS, MS and HS denotes low strain, medium strain and high strain, respectively. Note that insets a1 and d1 are in plane polarised light to better show the grain relationships.

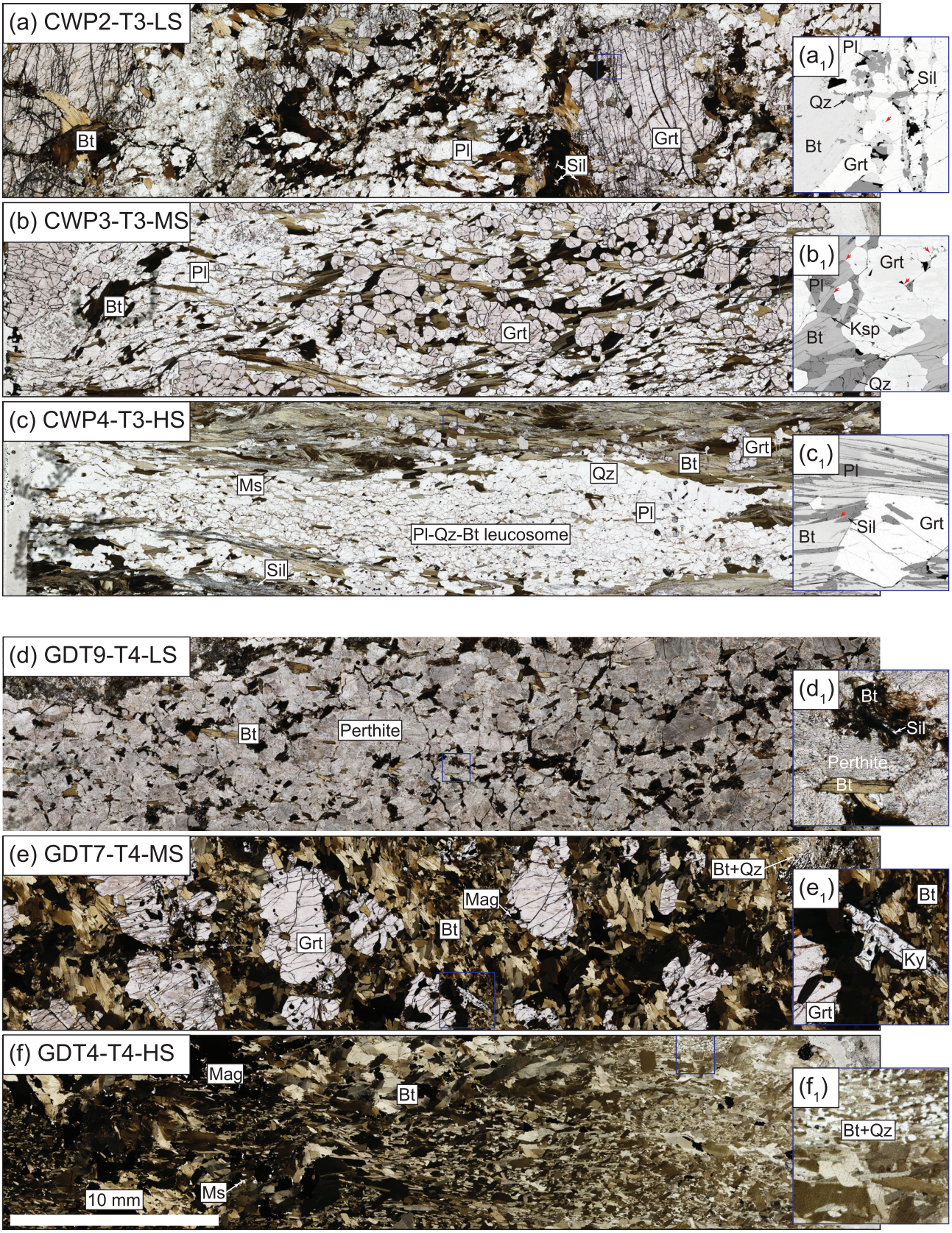

FIGURE 4 | Plane polarised light (PPL) photomicrograph overview images of the entire length of the thin sections of the 6 samples (transects 3 and 4) from the Strangways Range. Transects 3 and 4 are denoted as T3 and T4 while LS, MS and HS denotes low strain, medium strain and high strain, respectively. Note that insets a1–c1 are back-scattered electron images to better show the grain relationships.

TABLE 1 | Estimated modal proportions of minerals for the 12 samples from the four transects.

Sample name	Transect	Degree of strain	Rock type	Mineral modes (% from micro-XRF maps of entire thin section)													Comments
				Qz	Kfs	Pl	Grt	Bt	Sil	Ky	Mag	And	Chl	Ms	Crd	Rt	
R4	T1	LS	Crd Bt Sil gneiss	15	39	—	—	6.5	3	—	—	—	2	—	34		Crd rich with Bt inclusions and alterations
R6	T1	MS	Bt Chl Ms. schist	27	—	—	—	28	—	—	—	—	5	37.5	—	2	Schistose rock with elongated quartz
R8	T1	HS	Bt Qz And schist	29	—	—	—	27	—	—	—	31	12	—	—	—	Bt warping Qz bearing And porphyroblast
R26	T2	LS	Augen Gneiss	49.5	23	18	5	5	1	—	—	—	—	—	—	—	Stretched deformed Grt bearing gneiss
R29	T2	MS	Schistose granitic gneiss	41.5	15	27.5	—	7	—	—	—	—	—	9	—	—	Hydration of Pl,Kfs,Qz to Ms
R30	T2	HS	Chl Bt Rt schist	12	—	3.5	—	36	—	—	—	—	40	4	—	4	Highly schistose rock with patchy Rt
CWP 2	T3	LS	Garnet gneiss	9.5	—	33	31	24	1.5	—	—	—	—	—	—	—	Grt breakdown reaction textures
CWP 3	T3	MS	Grt Bt schist	2	—	49.5	36.5	12	—	—	—	—	—	—	—	—	Neoblasts of Grt with Pl films
CWP 4	T3	HS	Bt Sil schist	24	—	27	4	36	7	—	—	—	—	—	—	—	Highly schistose rock intruded by felsic vein
GDT 9	T4	LS	Grt-bearing felsic granulite	—	57	14	—	26	4	—	—	—	—	—	—	—	Perthitic Kfs with Bt reaction textures
GDT 7	T4	MS	Grt Bt schist	3	—	—	30	58	2	1	7	—	—	—	—	—	Grt Bt rich schist with aluminosilicates replacing Grt
GDT 4	T4	HS	Bt schist	1	—	—	—	80	7	—	13	—	—	—	—	—	2 generations of Bt; the latter possibly formed by replacing Grt like in GDT7

Note: R8 = RAN008 (abbreviated sample prefixes of Raimondo et al. 2011). Transects 1–4 are denoted as T1, T2, T3 and T4. LS, MS and HS denotes low strain, medium strain and high strain, respectively.
Abbreviations: And, andalusite; Bt, biotite; Chl, chlorite; Crd, cordierite; Grt, garnet; Kfs, K-feldspar; Ky, kyanite; Mag, magnetite; Ms, muscovite; Pl, plagioclase; Qz, quartz; Rt, rutile; Sil, sillimanite.

Some biotite grains are partially replaced by sillimanite, while others are replaced by chlorite, which is relatively minor (Table 1, Figure S1). Micaceous minerals and sillimanite exhibit no preferred orientation and are common within cordierite and K-feldspar grains as inclusions (Figure 3a). Metapsammitic samples outside the shear zone are enriched in quartz, with less cordierite, sillimanite and biotite compared with metapelitic samples.

Medium-strain rocks at the shear zone margins are biotite-chlorite-muscovite schist lacking cordierite, but containing kyanite (sample R6-T1-MS) and trace opaque minerals. The schistosity is well-defined by biotite (some altered to chlorite) and muscovite (Figures 3b and 5b), while second-generation muscovite grains crosscut the schistosity at a high angle. Microlithon domains consist of elongate quartz (with high aspect ratio), and some patchy rutile grains are hosted along the schistosity. Some quartz grains have undergone grain size reduction due to dynamic recrystallisation and occur as patches within the micaceous domains.

High-strain rocks at the centre of the shear zone are coarser grained and include biotite–quartz schist and biotite–quartz–andalusite schist (sample R8-T1-HS; Figures 3c and 5c). Minor deformed quartz veins (< 0.3 m thick) are observed in areas close to the high-strain zone. In the biotite–quartz–andalusite schist, the foliation wraps around coarse (3–6 mm) andalusite porphyroblasts. Biotite grains (< 0.5 mm) within the high-strain domains exhibit bending and undulose extinction (Figure 5d). Quartz grains (< 0.5 mm) show sutured grain contacts (Figure 5e). In another domain of the sample, quartz grains exhibit core and mantle structure along with recrystallisation (Figure 5f). Andalusite is absent towards the granitic orthogneiss (Anmatjira Orthogneiss) side of the shear zone (Figure 1d), providing confidence that three metasedimentary protoliths have been sampled in transect 1 within 200 m of each other.

4.2 | Reynolds Range, Unnamed Shear Zone in the Yaningidjara Hills (Transect 2, T2)

A distinct 150 m wide shear zone, steeply dipping to the north on the southeastern margin of the Yaningidjara Hills in the Reynolds Range, is characterised by biotite ± garnet schistose granitic gneiss. This shear zone cuts through homogeneous granitic augen orthogneiss that is exposed on both sides of the shear zone (Figure 1e). A single protolith is inferred for Transect 2, so the three rocks, collected from within 100 m of one another, are thought to have had the same initial bulk composition. Quartz veins, running subparallel to the shear foliation, are evident in the high-strain zone (Figure 1e and red arrow on Figure 2b). The shear zone exhibits a down-dip mineral

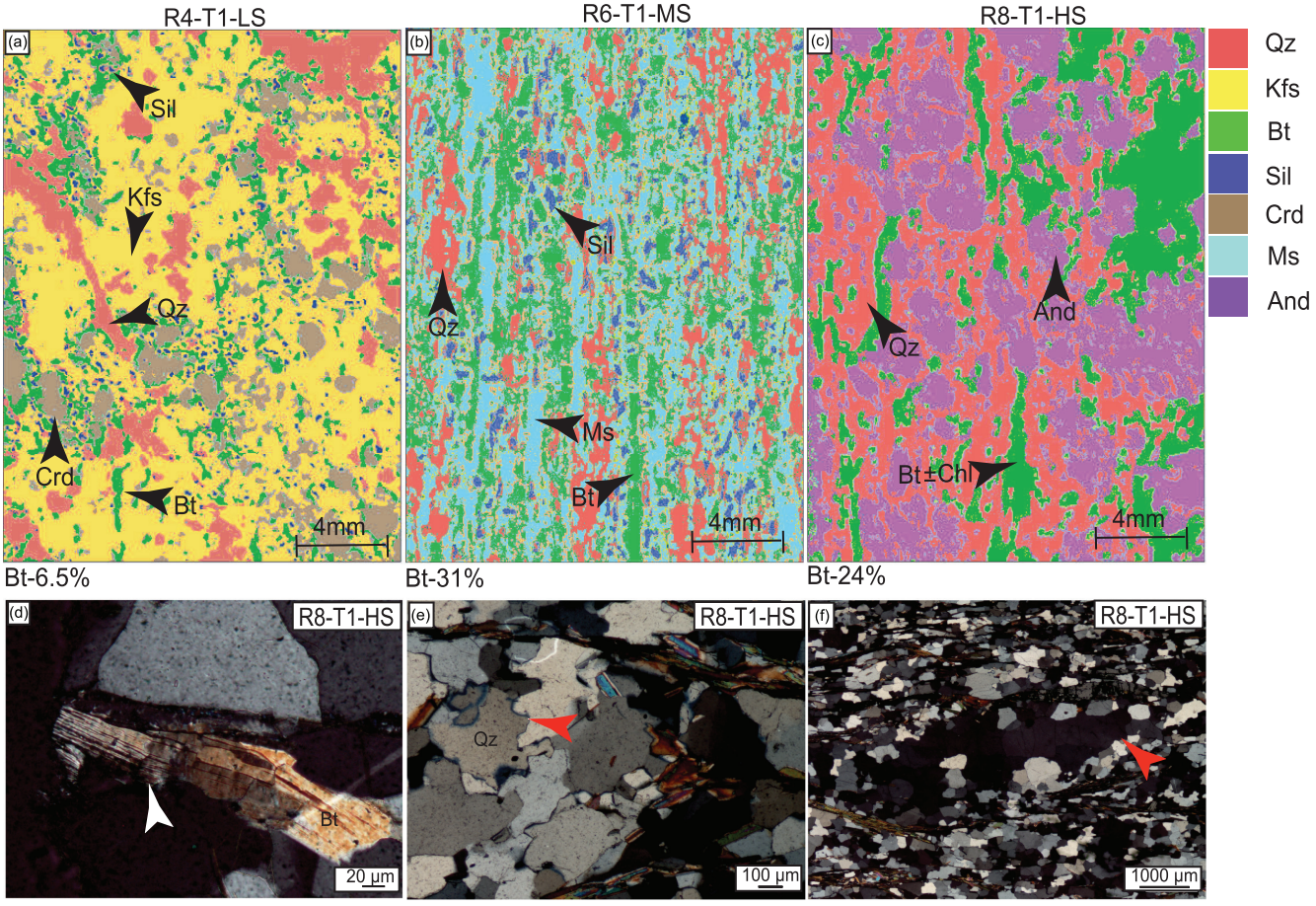

FIGURE 5 | (a–c) Micro-XRF phase maps of representative sections of (a) R4-T1-LS, (b) R6-T1-MS and (c) R8-T1-HS. (d–f) Photomicrographs (XPL) of sample R8-T1-HS that exhibit (d) a bent biotite grain against quartz grains, (e) sutured boundaries among quartz grains, and (f) core and mantle structure among quartz grains.

elongation lineation defined by aligned mica, and S–C fabrics and rotated porphyroclasts suggest a reverse sense of movement (top to the south).

The low-strain augen gneiss sample outside the shear zone is coarse-grained (1–3 mm) and comprises quartz with well-developed undulose extinction, plagioclase, perthitic K-feldspar augen, garnet and biotite with minor myrmekite at K-feldspar grain boundaries (sample R26-T2-LS; Figure 3d) and accessory opaque minerals. Biotite grains are mainly found at the periphery of highly deformed and elongate garnet grains (Figures 3d and 6a).

Two samples of medium to high-strain rocks were examined, including medium-strain mylonitic biotite ± garnet schistose granitic gneiss (sample R29-T2-MS; Figures 3e and 6b) and a high-strain rare chlorite biotite–rutile schist (sample R30-T2-HS; Figures 3f and 6c) that only occurs adjacent to quartz veins. The higher-strain domains in Transect 2 exhibit similar but finer-grained recrystallised quartz and plagioclase grains along with highly strained coarser grains (Figure 6b,d–f), compared with Transect 1. The mode of biotite and chlorite significantly increases with the rising strain (Table 1, Figure S1) and all samples contain accessory opaque minerals. Muscovite grains lack a preferred orientation and are commonly alteration products of other grains (quartz and plagioclase), occurring in a random pattern throughout the rock. Preserved textures suggest preferential alteration along weak zones such as grain boundaries and fractures. Plagioclase and quartz exhibit ragged boundaries against the muscovite domains (Figure 6d). Quartz grains display a bimodal grain size distribution due to patches of recrystallised grains near hydration zones (Figure 6e). Plagioclase grains show evidence of brittle fracture with later quartz infilling (Figure 6f). Schistosity in the rare chlorite–biotite–rutile schist, located adjacent to recrystallised quartz veins, is defined by biotite, chlorite and muscovite (Figure 6c), with fine rutile occasionally forming clusters along the schistosity.

4.3 | Strangways Range, Cattle Water Pass Shear Zone (Transect 3, T3)

In the eastern Strangways Range, a prominent 100–300 m wide shear zone, steeply east- to south-dipping and displaying strong anastomosing features, is characterised by sillimanite–garnet–biotite schist (Figure 1c,f). Cutting through Proterozoic mafic, felsic and pelitic granulites, the shear zone envelops pods of variably modified granulite. Higher strain domains within the felsic granulite reveal the gradual development of anastomosing layers rich in biotite ± muscovite (Figure 2c,d), while mafic granulite protoliths transform into rocks rich in amphibole ± garnet. High strain rocks manifest as mica schist with mylonitic fabrics,

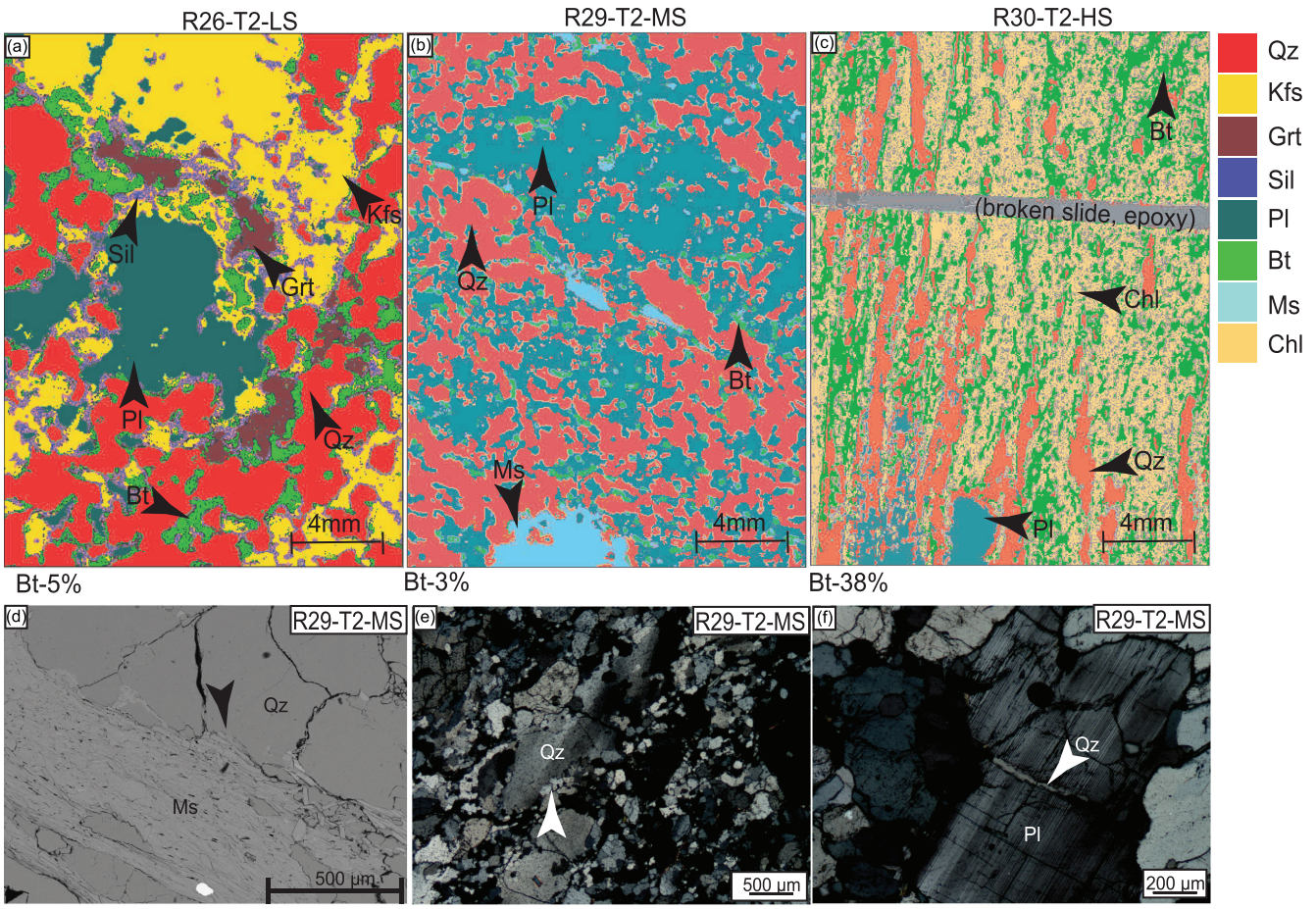

FIGURE 6 | (a–c) Micro-XRF phase maps of representative sections of (a) R26-T2-LS, (b) R29-T2-MS and (c) R30-T2-HS. (d–f) Back-scattered electron image and photomicrographs (XPL) of sample R29-T2-MS that exhibit (d) ragged grain boundaries of quartz, partially replaced and hydrated to muscovite, (e) high undulosity and recrystallisation of quartz grains, and (f) fractured plagioclase infilled with quartz.

featuring asymmetric strain shadows (σ type) and S–C fabrics indicative of a reverse sense of movement (top to the west).

Transect 3 samples low-strain garnet gneiss and high-strain garnet–biotite schists. Amphibole is absent, and aluminosilicate minerals are of low mode in all three samples, implying a felsic granulite protolith for each sample in Transect 3, all collected within 150 m of each other (Figure 1f). The low-strain granulite (CWP2-T3-LS) hosts relict plagioclase (Pl1; 1–1.5 mm), garnet (Grt1; 4–6 mm), biotite (Bt1) and quartz (Qz1) (Figures 4a and 7a) and accessory opaque minerals. Fractures in the garnet grains are filled with finer plagioclase, sillimanite, quartz and biotite (red arrow, Figure 8a), and within the garnets, these fractures connect to microgranitoid pockets defined by quartz, plagioclase and biotite (Figure 8a). Minor modification of the low-strain sample includes fine-grained textures cutting and partially replacing the relict granulite minerals. Along the fractures, granulite garnet (Grt1) is cut by fine biotite (0.5–0.7 mm; Figure 4a and red arrow in Figure 8b) or biotite ± sillimanite ± plagioclase ± quartz (< 0.1 mm), and the rims of Grt1 are partially replaced by biotite, plagioclase, quartz and minor sillimanite (< 0.7 mm). The biotite grains are wider near Grt1 grain boundaries and gradually branch out and become thinner within the garnet (Figure 8b). Granulite-facies plagioclase (Pl1) is distinguished by grain size from fine cuspate plagioclase grains, which appear to have formed due to later-stage reactions (Pl2; 0.4–0.6 mm) (Figure 8a,b).

The medium strain domain of Transect 3 (sample CWP3-T3-MS) comprises schist with garnet (Grt2; 0.5–1 mm), plagioclase (Pl2; < 0.5 mm) and biotite (Bt2; < 0.5 mm, red arrow in Figure 2c) with trace accessory opaque minerals. Schistosity is defined by biotite, although in places, biotite shows more random orientations (Figures 4b and 7b). Grt2 grains lack inclusions and have well-developed crystal faces, forming in aggregates (Figure 8c,d). Low apparent dihedral angles (< 60°, red arrow, Figure 8c,d) and films (0.2–0.3 mm long; black arrow, Figure 8c) of felsic minerals are common between garnet grains. Interstitial plagioclase within aggregates of garnet may have the same extinction position, consistent with having one crystallographic orientation (red arrows, Figure 8d). High-resolution BSE images show minor quartz and K-feldspar in addition to Pl2, forming an interlocking texture (red arrow, Figure 8e). Two subtly different BSE-response K-feldspar grains are observed, possibly due to multiple stages of K-feldspar growth. Plagioclase is rarely partially replaced by sillimanite (highlighted red circle and inset, Figure 8e). Under higher magnification, finger-like protrusions of sillimanite into the plagioclase are observed (black arrow, inset, Figure 8e). Along the grain boundaries of plagioclase, quartz forms a 'string of bead' texture (Holness et al. (2011); black arrows, Figure 8f). Higher magnification shows that some of these quartz grains crystallised at triple junctions of plagioclase grains (red arrow, inset, Figure 8f). Rare granitic veins intrude the high strain domain of the Cattle Water Pass shear zone (CWP4-T3-HS, Figure 4c). Quartz and plagioclase in the veins are coarse-grained (1–2 mm) and are not deformed. Biotite–sillimanite–rich layers are common in high-strain domains and contain mica fish and trace opaque minerals. Garnet (Grt3; 0.5–1 mm) with prominent crystal faces decorates the schist at the contact with the granitic veins (Figure 7c).

4.4 | Strangways Range, Gough Dam Shear Zone (Transect 4, T4)

To the north of the Cattle Water Pass shear zone lies a substantial shear zone, named the Gough Dam schist zone, with a thickness ranging from 600 m to over 1 km, and it dips northward (Figure 1c,g; Norman 1991). Comprising phyllonitic quartzofeldspathic gneiss and biotite schists (Ballevre et al. 1997; Piazolo et al. 2020; Silva et al. 2022), the zone exhibits steeply northeast-plunging quartz rods and mineral lineations (biotite–sillimanite), occasionally featuring locally observed kyanite. While porphyroclasts generally exhibit symmetrical flattening, rare σ-type strain shadows suggest a reverse sense of movement (top to SW).

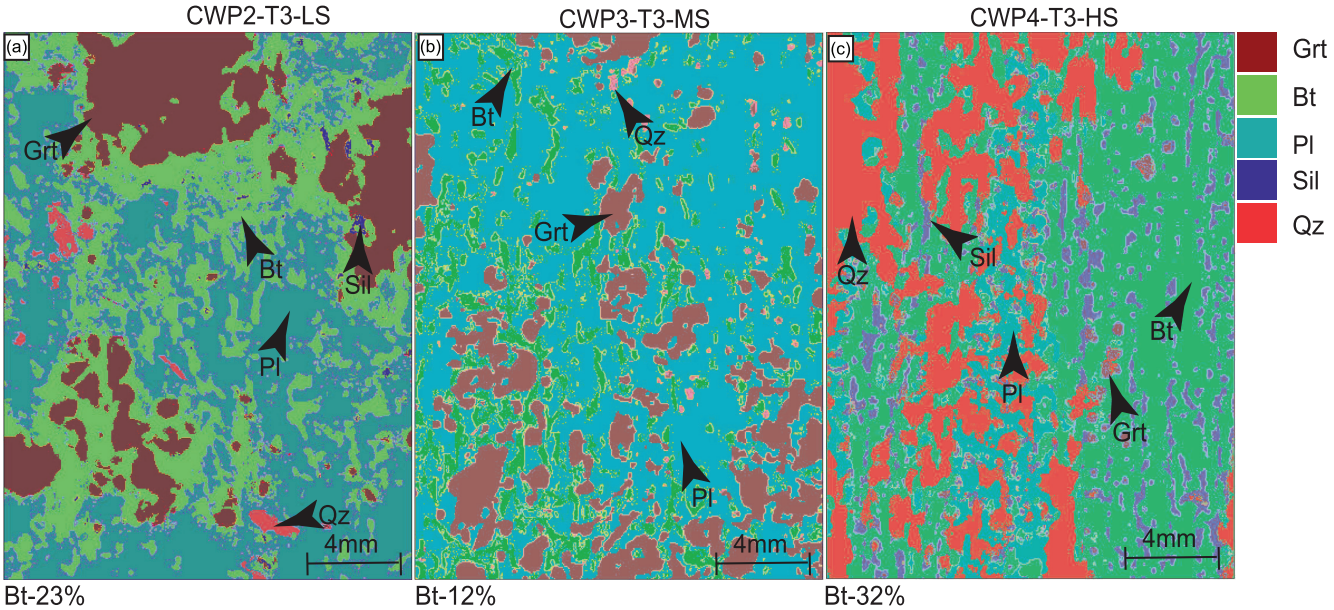

FIGURE 7 | (a–c) Micro-XRF phase maps of representative sections of (a) CWP2-T3-LS, (b) CWP3-T3-MS and (c) CWP4-T3-HS.

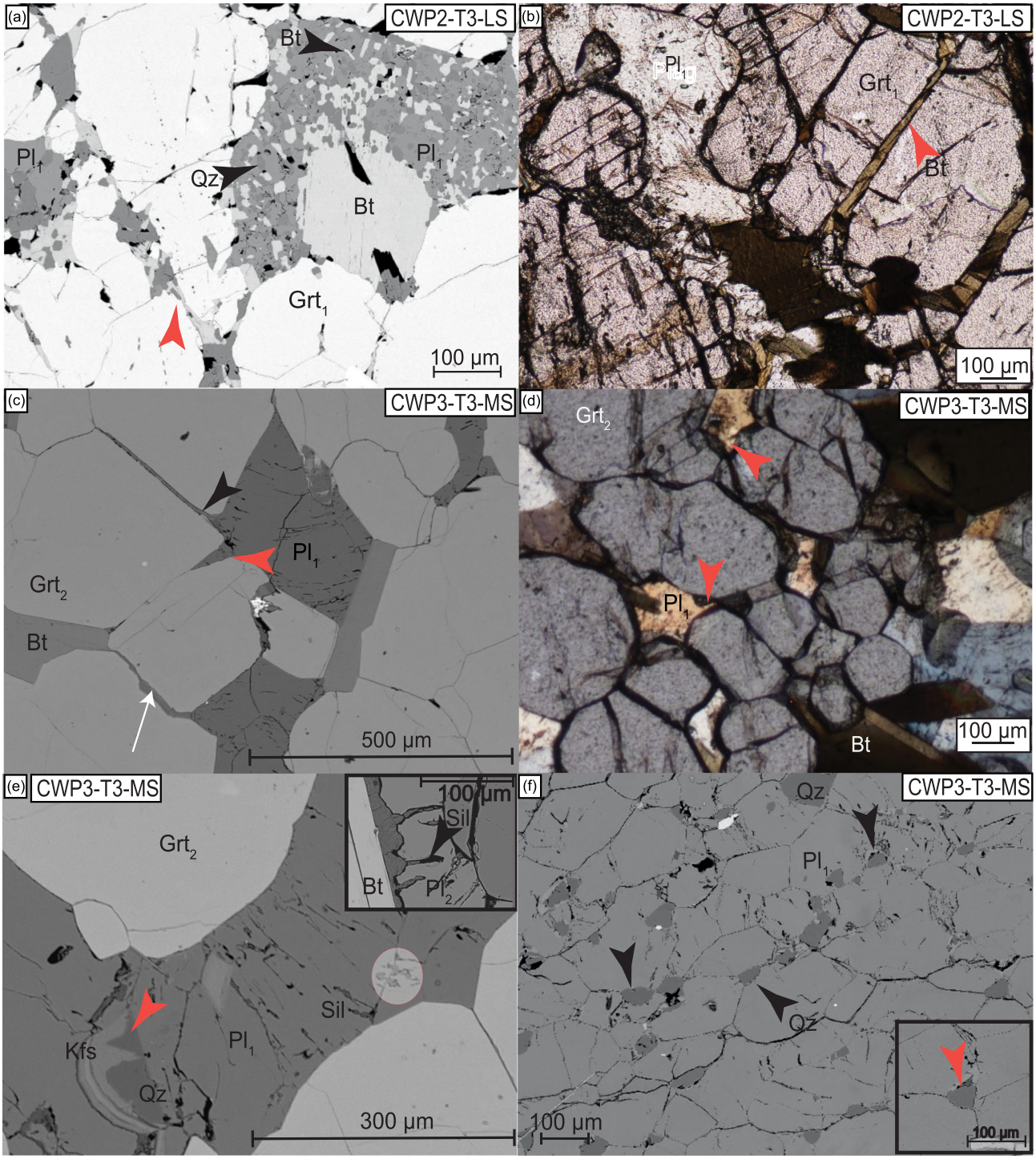

FIGURE 8 | Back-scattered electron images and photomicrographs illustrating microstructures indicative of the former presence of melt within the shear zone in T3. (a) Sample CWP2-T3-LS preserves microgranite within granulite facies garnets. (b) Sample CWP2-T3-LS (PPL) exhibits garnet grains partially altered to biotite along cracks and plagioclase with a cuspate texture. (c) Sample CWP3-T3-MS exhibits low apparent dihedral angles and elongate films along the garnet grain boundaries. (d) Sample CWP3-T3-MS (XPL) exhibits plagioclase grains between garnet grains having low apparent dihedral angles and sharing the same extinction position. (e) Sample CWP3-T3-MS exhibits three-mineral assemblage depicted by the growth of interlocking K-feldspar and quartz along with plagioclase and inset shows sillimanite protrusions replacing plagioclase along twins. (f) Sample CWP2-T3-MS exhibits 'string of beads' of quartz along margins of plagioclase and inset shows a quartz grain at the triple junction of plagioclase grains.

Throughout the schist belt, remnants of granulite pods are evident. These granulite formations undergo partial replacement by a biotite-rich rock along the margins and fractures of the pods. The sheared rocks encasing the pods showcase syn-tectonic granitic lenses, veins and dykes (Figure 2e,f), characterised by coarse, interlocking, euhedral grains, even at the tapered margins of the lenses. Notably, biotite selvedges are present along the boundaries of the granitic components (yellow arrow, Figure 2f).

Transect 4, the shortest among our transects, commences in garnet-bearing felsic granulite (GDT9-T4-LS; Figures 4d and 9a) and concludes in biotite schist (GDT4-T4-HS; Figures 4f and 9c), intruded by granitic veins. All three samples, within a 5 m range, are carefully chosen to ensure representation from a single protolith. The low-strain sample consists of coarse perthitic K-feldspar (~2 mm) and patchy biotite (< 1 mm). Biotite grains exhibit alteration and growth of finer biotite grains along the margins (Figure 4d). In the medium-strain domain (GDT7-T4-MS), the mineral assemblage comprises biotite and garnet (3–8 mm), with minor kyanite (~2 mm), sillimanite (0.5–4 mm) and magnetite (Figures 4e and 9b). The biotite grains lack a preferred orientation throughout the schist. The highly modified high-strain rock from the Gough Dam shear zone (GDT4-T4-HS) is compositionally like GDT7-T4-MS, predominantly composed of biotite and magnetite, but lacks the coarse garnet (Figures 4f and 9c). Both the medium and high-strain domains contain quartz–biotite symplectite (Figure 9d,e). Finer-grained biotite (0.2–0.7 mm) makes up most of the rock, and sillimanite and magnetite (1–1.5 mm) constitute < 30% (Table 1, Figure S1). The finer biotite grains lack any preferred orientation, like GDT7-T4-MS, while coarser biotite grains are slightly more aligned. Coarse biotite grains occur as clusters within the sample, and they are oriented differently in each of these clusters. Regions of coarse biotite (Bt) grains (2–4 mm) may have pseudomorphed garnet, with these domains exhibiting a similar size and shape to the garnet grains observed in GDT7-T4-MS.

5 | Major, Trace and Rare Earth Element Geochemistry

To explore the mobility of elements and the extent of chemical changes within each shear zone, we conducted a comprehensive analysis of whole rock geochemical data. Despite our careful efforts to sample a single protolith in each transect, variations can arise, particularly in metasedimentary packages, as opposed to metaigneous rocks. Therefore, in the ensuing evaluation of geochemical patterns, we emphasise significant differences between samples and highlight those exhibiting unusual geochemical patterns. Additionally, a section on elemental ratio and Gresens' analysis is presented in the Supplementary materials to scrutinise the practicality and limitations of such plots in comparing aqueous fluids versus silicate melts.

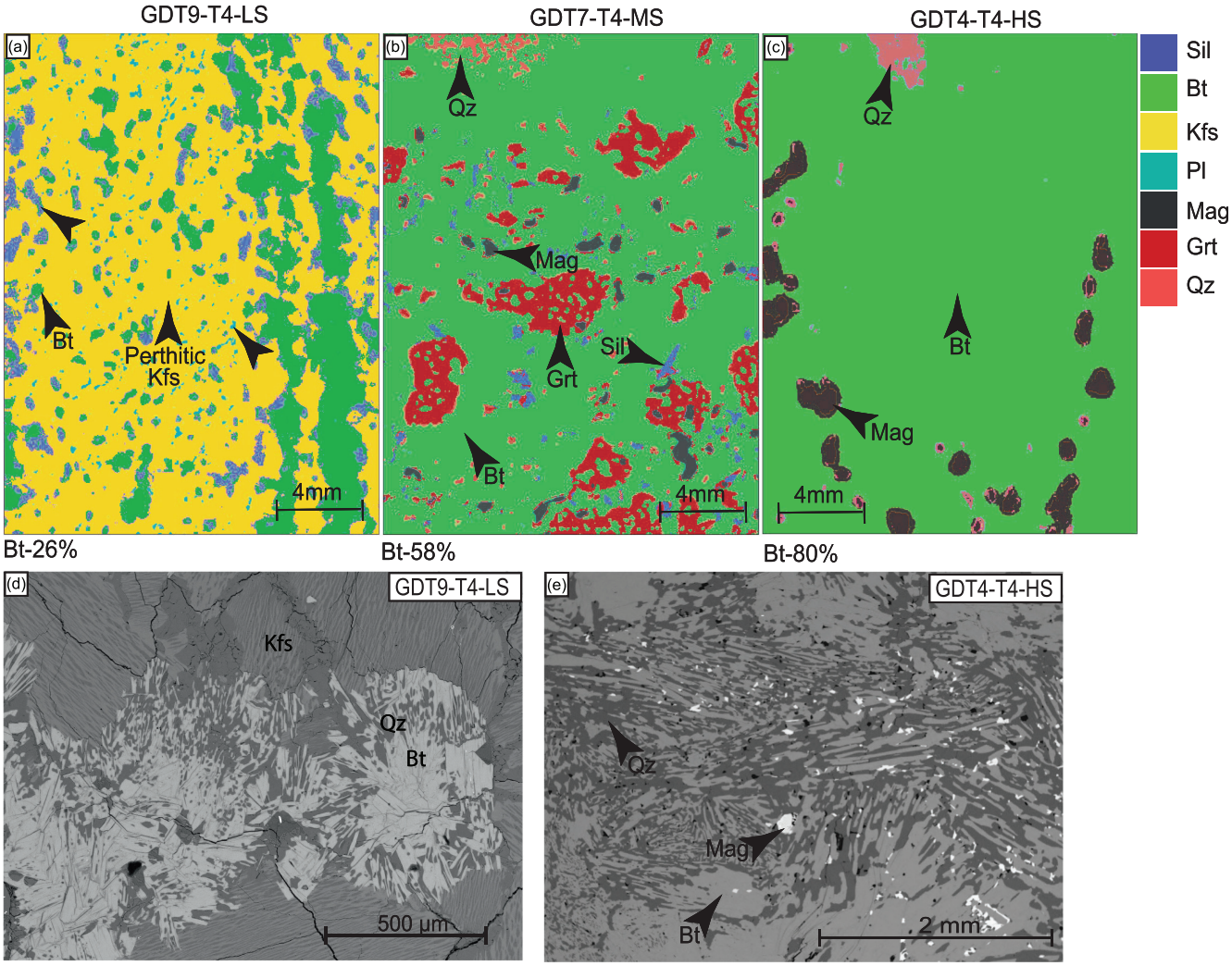

FIGURE 9 | (a–c) Micro-XRF phase maps of representative sections of (a) GDT9-T4-LS, (b) GDT7-T4-MS and (c) GDT4-T4-HS. (d, e) Back-scattered electron images of (d) sample GDT9-T4-LS and (e) sample GDT4-T4-HS both exhibiting quartz–biotite symplectite.

5.1 | Major Elements

Consistent trends between the inferred degree of strain and major element data are scarce, except for notable exceptions such as CaO and Na_2O. These elements are depleted in high-strain samples compared to low-strain counterparts in all four transects, primarily due to feldspar replacement. Transects T1 (Anmatjira Range) and T3 (Strangways Range) show the least modification of major element chemistry, while high-strain samples in T2 (Reynolds Range) and T4 (Strangways Range) exhibit substantial changes in major element chemistry compared to low-strain rocks (Figure 10). Figures S2 and S3 illustrate the relative mobility, enrichment and depletion patterns of major elements.

5.2 | Trace Elements

Trace element concentrations (Table 2), normalised to C1 chondrite values from McDonough and Sun (1995), are plotted for transects T1 and T2 (Reynolds–Anmatjira Ranges) and T3 and T4 (Strangways Range) in Figure 11. Notably, samples from within each transect share similar trace element patterns. Specific observations include the enrichment of the high-strain sample in T1 (R8-T1-HS) in all trace elements, including Zr and Hf which are 20–30 times the LS and MS samples. This contrasts with the minor depletion seen in the medium-strain sample in T2 (R29-T2-MS). The Cu and Sn values in R29-T2-MS are relatively enriched compared to the other two samples in T2. Higher concentrations of cobalt compared to nickel are evident

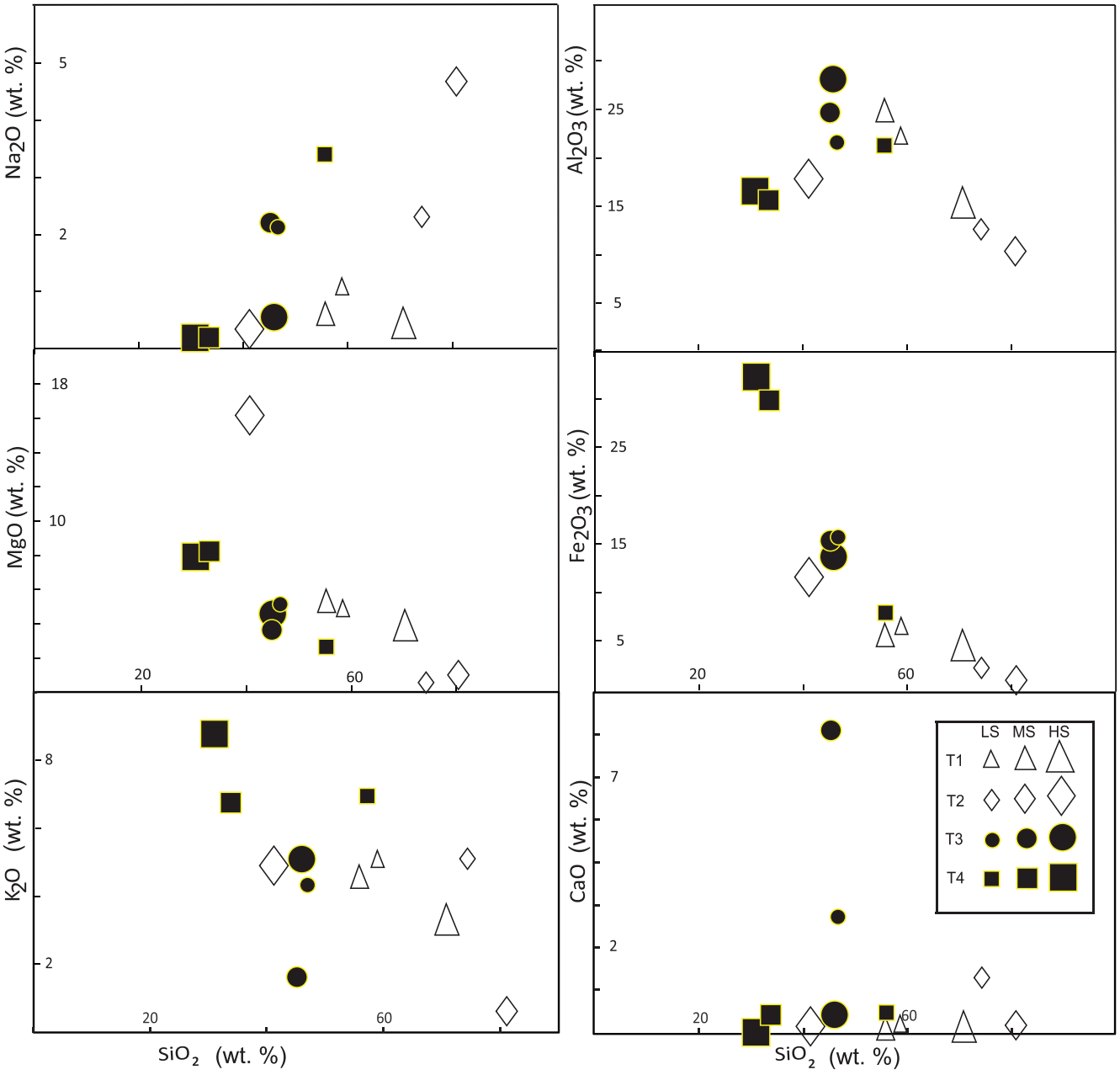

FIGURE 10 | Whole rock major element weight percent (wt. %) oxides (Na_2O, MgO, Al_2O_3, Fe_2O_3, K_2O and CaO) versus SiO_2 (wt. %) for all 12 samples from the four transects. Transects 1–4 are denoted as T1, T2, T3 and T4. LS, MS and HS denotes low strain, medium strain and high strain, respectively.

TABLE 2 | Whole rock trace element data (LA-ICPMS; parts per million – ppm).

Sample		R4	R6	R8	R26	R29	R30	CWP2	CWP3	CWP4	GDT9	GDT7	GDT4
Transect		T1	T1	T1	T2	T2	T2	T3	T3	T3	T4	T4	T4
Degree of strain		LS	MS	HS	LS	MS	HS	LS	MS	HS	LS	MS	HS
V	ppm	94.5	63.13	594.34	21.04	24.21	255.06	167.02	101.83	128.31	67.29	599.62	26.22
Cr	ppm	83.6	57.26	620.42	28	7.74	41.68	182.88	118.94	121.1	69.57	279.67	21.85
Co	ppm	32.35	36.45	832.4	111.03	2.83	66.91	32.03	30.96	22.7	14.65	83.37	3.06
Ni	ppm	34.17	31.41	243.2	21.42	9.24	123.6	66.17	40.11	56.98	33.84	172.05	6.9
Cu	ppm	4.01	1.89	64.85	8.55	6.58	2.98	18.17	7.56	7.12	14.98	202.01	0.661
Zn	ppm	42.63	10.27	305.5	32.06	2.93	29.13	64.13	31.04	73.1	24.31	85.05	4.6
Ga	ppm	65.76	48.92	389.05	40.1	10.2	33.95	72.48	41.22	68.36	58.73	96.64	4.63
Rb	ppm	189.41	113.99	1337.8	272.99	19.63	400.64	197.47	83.71	128.76	140.57	342.29	26.92
Sr	ppm	29.41	18.61	< 156.40	73.37	4.72	16.75	85.15	166.82	21.3	38.07	< 10.71	< 0.56
Y	ppm	26.8	20.68	230.59	34.78	20.86	14.06	33.17	147.24	19.69	46.92	51.51	1.71
Zr	ppm	166.76	124.2	2414.61	153.96	66.03	126.29	298.04	304.36	162.67	92.71	260.19	5.03
Nb	ppm	18.71	12.25	100.6	8.5	4.85	6.54	16.83	4.51	13.23	9.39	40.8	0.735
Ag	ppm	< 0.175	0.095	2.78	0.39	0.117	0.581	0.527	0.169	1.58	0.587	2.1	0.0233
Sn	ppm	4.93	< 1.79	< 20.47	5.86	9.37	11.55	4.48	3.94	2.98	13.35	27.19	1.92
Cs	ppm	2.59	2.3	27.13	2.26	0.142	7.95	1.134	0.479	0.681	0.32	1.19	0.1361
Ba	ppm	546.61	534.06	3504.32	409.16	26.68	172.71	938.4	317.55	668.98	816.4	877.26	51.67
Hf	ppm	3.83	3.36	58.92	4.84	2.18	3.03	7.73	8.52	3.25	2.58	6.08	0.141
Ta	ppm	1.81	1.15	14.76	1.277	0.489	0.688	1.049	0.19	0.762	0.553	2.07	0.042
Au	ppm	30.61	14.44	337.51	45.8	23.49	31.19	24.02	22.06	16.99	22.1	44.5	1.75
Pb	ppm	11.36	2.79	56.48	33.4	2.36	1.69	12.07	2.37	4.04	18.35	9.81	0.145
Th	ppm	24.02	19.19	284.38	32.49	13.89	2.22	0.313	8.23	19.86	18.01	3.96	0.0139
U	ppm	5.47	2.4	45.25	4.05	1.79	1.32	0.387	0.514	0.393	0.835	0.394	0.0157

Note: R = RAN008 (abbreviated sample prefixes of Raimondo et al. 2011). Transects 1–4 are denoted as T1, T2, T3 and T4. LS, MS and HS denotes low strain, medium strain and high strain, respectively.

in all samples, but these elements are more variable in medium- and high-strain rocks (2.83–832.4 ppm Co; 9.24–243.2 ppm Ni) compared to low-strain rocks (32.35–111.03 ppm Co; 21.42–34.17 ppm Ni). The three samples in T3 share grossly similar trace element patterns (Figure 11). In T4, the high-strain sample (GDT4-T4-HS) is depleted in all trace elements compared to the low-strain sample (GDT9-T4-LS), whereas the garnet-bearing medium-strain sample (GDT7-T4-MS) is relatively enriched in most trace elements (except for Pb, Th and U). Like T1 and T2, Ni shows a wide range of values within the high-and medium-strain samples of T4 (6.9–172.05 ppm), whereas the low-strain samples from T3 and T4 vary less (33.84–66.17 ppm).

The observations above indicate that neither the samples from the Reynolds–Anmatjira Ranges (T1 and T2) nor Strangways Range (T3 and T4) show any consistent trends in trace element patterns when comparing LS, MS and HS samples within each transect. T2 and T3 do not significantly change trace element concentrations in high strain samples compared to their low strain counterparts. However, T2 stands out with remarkable changes for Sn and Cs and T3 for Y, Hf, Ta and Th. Transects 1 and 4 show opposing trends of enrichment and depletion between sheared and unsheared samples, respectively. The relative mobility of Zr and Hf has been discussed in further detail in the supplementary section on Gresens' analysis.

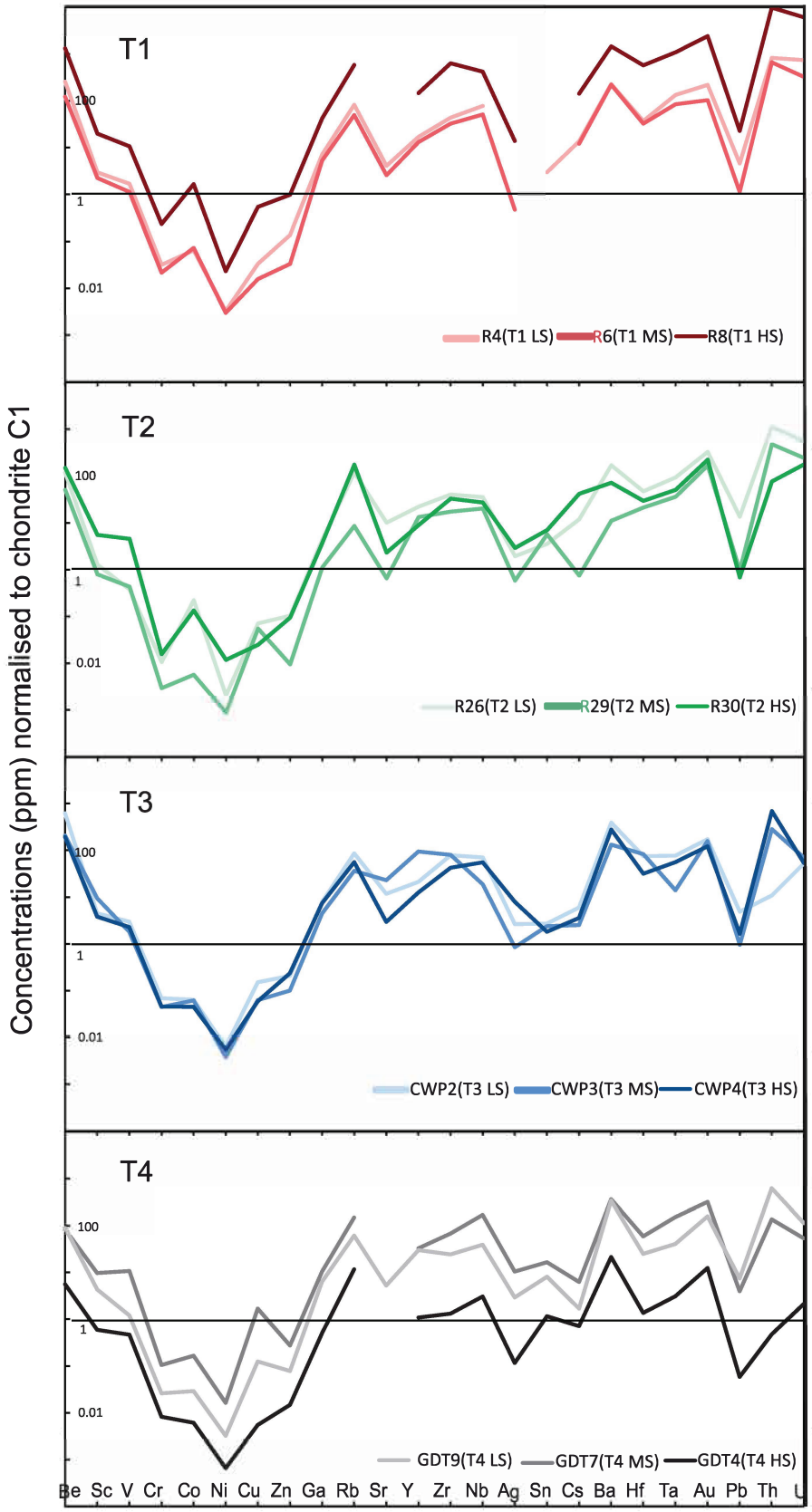

FIGURE 11 | Whole rock trace element concentrations normalised to chondrite C1 for all 12 samples from the 4 transects. Transects 1–4 are denoted as T1, T2, T3 and T4. LS, MS and HS denotes low strain, medium strain and high strain, respectively.

TABLE 3 | Whole rock rare earth element analysis (LA-ICPMS; parts per million – ppm).

Sample		R4	R6	R8	R26	R29	R30	CWP2	CWP3	CWP4	GDT9	GDT7	GDT4
Transect		T1	T1	T1	T2	T2	T2	T3	T3	T3	T4	T4	T4
Degree of strain		LS	MS	HS	LS	MS	HS	LS	MS	HS	LS	MS	HS
La	ppm	56.64	50.52	454.37	40.13	17.19	10.12	33.94	38.2	56.64	46.38	19.9	0.0487
Ce	ppm	125.73	95.79	993.63	90.3	38.63	20.76	44.8	69.37	103.48	85.87	38.56	0.0929
Pr	ppm	13.22	11.31	109.01	9.2	4.17	2.76	4.03	6.75	10.42	9.24	4.1	0.008
Nd	ppm	42.62	42.92	356.26	32.82	15.12	12.07	14.26	26.55	40.69	33.55	16.39	0.0142
Sm	ppm	7.74	7.92	59.5	7.73	3.42	3.2	4.11	5.17	6.25	6.46	5.67	0.082
Eu	ppm	1.27	0.96	7.61	0.92	0.303	0.473	2.13	1.73	1.467	1.63	0.453	0.0199
Gd	ppm	6.67	4.96	51.43	6.62	3.19	2.97	4.51	7.75	4.74	5.56	8.72	0.229
Tb	ppm	0.818	0.644	6.33	0.907	0.562	0.543	0.98	2.3	0.652	1.047	1.504	0.0396
Dy	ppm	5.06	3.91	42.9	5.98	3.69	2.76	6.69	21.77	4.29	7.23	10.53	0.301
Ho	ppm	1.05	0.83	7.56	1.129	0.813	0.646	1.25	5.34	0.817	1.775	2.14	0.0617
Er	ppm	2.57	1.99	24.23	3.26	2.18	1.22	2.81	14.39	2.11	5.4	4.73	0.18
Tm	ppm	0.359	0.305	3.2	0.471	0.3	0.131	0.444	2.33	0.231	0.808	0.664	0.0301
Yb	ppm	2.06	1.82	19.79	3.06	1.78	1.38	2.3	16.46	2.19	6.59	3.83	0.214
Lu	ppm	0.337	0.216	2.14	0.348	0.244	0.209	0.384	2.19	0.309	1.005	0.491	0.031

Note: R = RAN008 (abbreviated sample prefixes of Raimondo et al. 2011). Transects 1–4 are denoted as T1, T2, T3 and T4. LS, MS and HS denotes low strain, medium strain and high strain, respectively.

5.3 | Rare Earth Elements (REE)

REE concentrations, normalised to C1 chondrite values (Table 3), are plotted for each transect in Figure 12. Samples from the Reynolds–Anmatjira Ranges exhibit broadly similar REE patterns (i.e., shape), although T2 samples show slightly flatter profiles, and the high-strain rock in T1 displays higher REE content. In contrast, samples from the Strangways Range reveal highly variable REE patterns within individual transects. For instance, the medium-strain rock in T3 has a concave-up REE pattern, while the high-strain rock in T4 is strongly depleted in all REE, especially Nd relative to Sm.

To facilitate comparison, REE concentrations in MS and HS samples were normalised to their respective LS counterparts. Values close to 1 indicate minimal absolute differences, and consistent values across elements suggest similar pattern shapes at different absolute concentrations. The standard deviation of these normalised values provides a simple metric for comparing pattern similarity. Transects 1 and 2 have standard deviations of ~20%–25%, indicating relatively consistent REE patterns and low REE mobility during deformation. In contrast, T3 and T4 show much higher variability (standard deviations of 40%–65%), suggesting greater REE mobility during deformation in these transects.

The rare earth element ratios La/Yb plotted against Gd/Yb (Figure 13) reinforce the clustering of samples in transects 1 and 2 from the Reynolds–Anmatjira Ranges and diverse REE patterns in transects 3 and 4 from the Strangways Range.

6 | Discussion

This discussion integrates field and microstructural observations with geochemical data to contrast two lower grade transects across shear zones in the Reynolds–Anmatjira Ranges (T1 and T2; Raimondo et al. 2011) with two higher grade transects spanning the Cattle Water Pass (Ghatak et al. 2022) and Gough Dam shear zones (T3 and T4; Piazolo et al. 2020, Silva et al. 2022) in the Strangways Range.

6.1 | Timing of Fluid Flow Relative to Deformation

The high strain zones exhibit a pronounced hydrous character, suggesting the influx of fluids, either in the form of water or melt. The absence of minerals displaying random static overgrowth textures rules out post-deformational fluid–rock interaction. Conversely, features associated with fluid fluxing, such as quartz veins, leucosome veins and lenses, and delicate melt microstructures, would not withstand the high strain deformation evident in the field relationships if the fluids were introduced prior to tectonic activity. Consequently, the fluid–rock interaction is interpreted to be syn-tectonic. This interpretation is supported by several lines of evidence: (i) the localisation of hydration to shear zones, (ii) the pronounced alignment of hydrous minerals defining the foliation and lineation, and (iii) the presence of quartz veins exhibiting a spectrum of deformed and undeformed varieties in both outcrop and thin section, indicating vein formation at different stages of deformation.

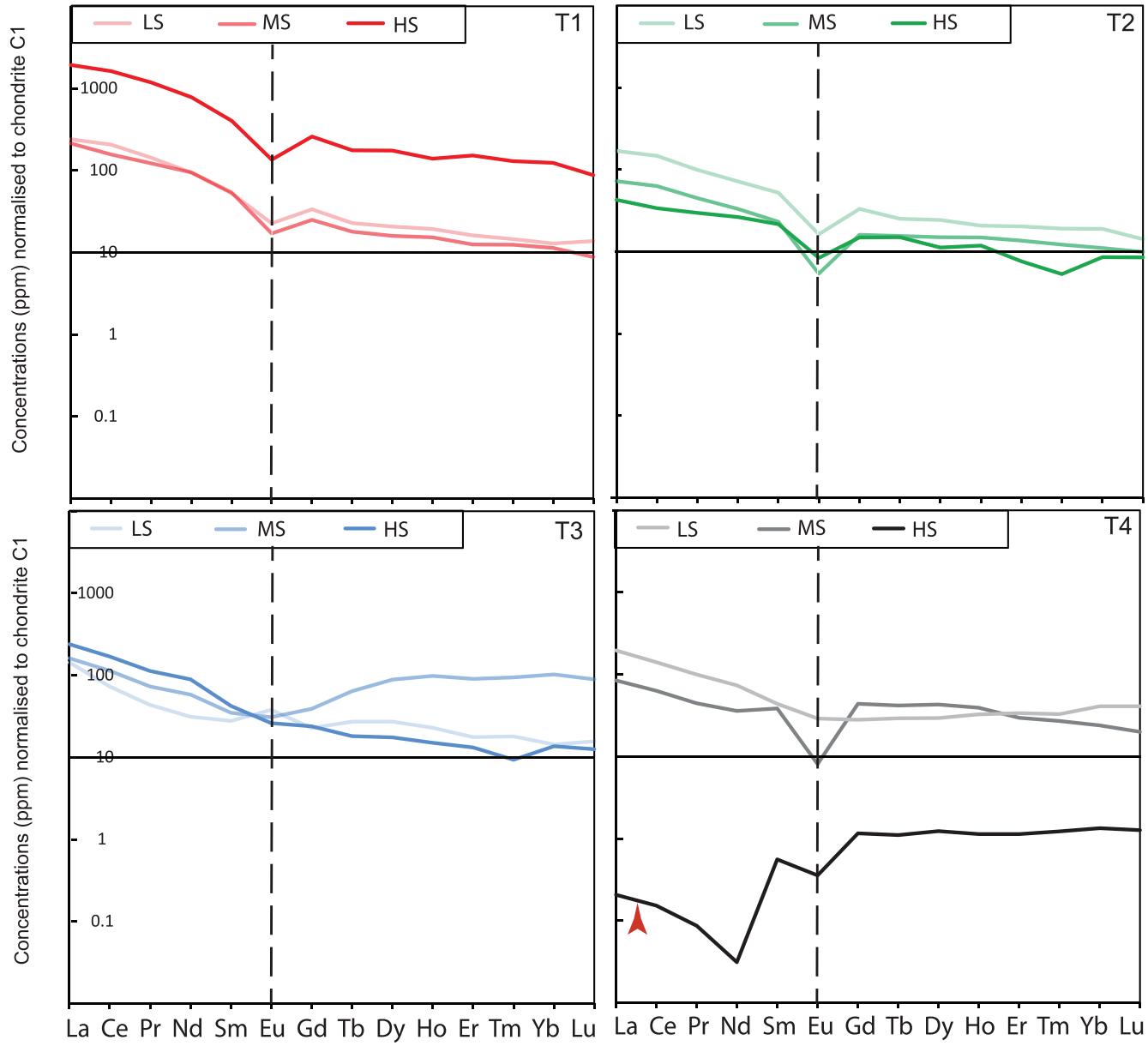

FIGURE 12 | Whole rock rare earth element concentrations normalised to chondrite C1 for all 12 samples from the 4 transects. Transects 1–4 are denoted as T1, T2, T3 and T4. LS, MS and HS denotes low strain, medium strain and high strain, respectively.

6.2 | Hydration Driven by Aqueous Fluid Versus Silicate Melt

6.2.1 | Field Relationships

The shear zones investigated (Figure 1b) are characterised by schist belts displaying hydrous mineral assemblages that cut through granulite facies precursor rocks. In the Reynolds–Anmatjira Ranges, shear zones exhibit an assemblage containing biotite, muscovite ± chlorite (Figure 3), while in the higher-grade shear zones of the Strangways Range, common constituents include biotite, garnet, sillimanite and K-feldspar (Figure 4). Foliation-parallel quartz veins, up to 3–5 m wide, are frequently observed in shear zones of the Reynolds–Anmatjira Ranges (red arrow, Figure 2b) and are boudinaged (Raimondo et al. 2011). In contrast, shear zones in the Strangways Range and nearby Harts Range feature syn- to post-tectonic pegmatite dykes (Buick et al. 2008, Silva et al. 2022), felsic dykes (red arrow, Figure 2e) and granite leucosome lenses (red arrow, Figure 2f; Piazolo et al. 2020). Adjacent to quartz veins (T2) or felsic dykes/lenses (T4) in the shear zones, reaction and metasomatism intensify, resulting in the common occurrence of biotite-rich selvedges (yellow arrow, Figure 2f).

Metamorphic and igneous dewatering serve as crucial sources of aqueous fluid rich in dissolved silica. These fluids propagate through hydro-fracturing, precipitating quartz as pressure or temperature decreases, thereby altering and hydrating wall rocks and forming quartz veins (Bons 2001). Ductile deformation aids the migration of silicate melt (Brown 1994; Stuart, Meek, et al. 2018), with melt inferred to move through percolative flow parallel to the maximum principal finite elongation

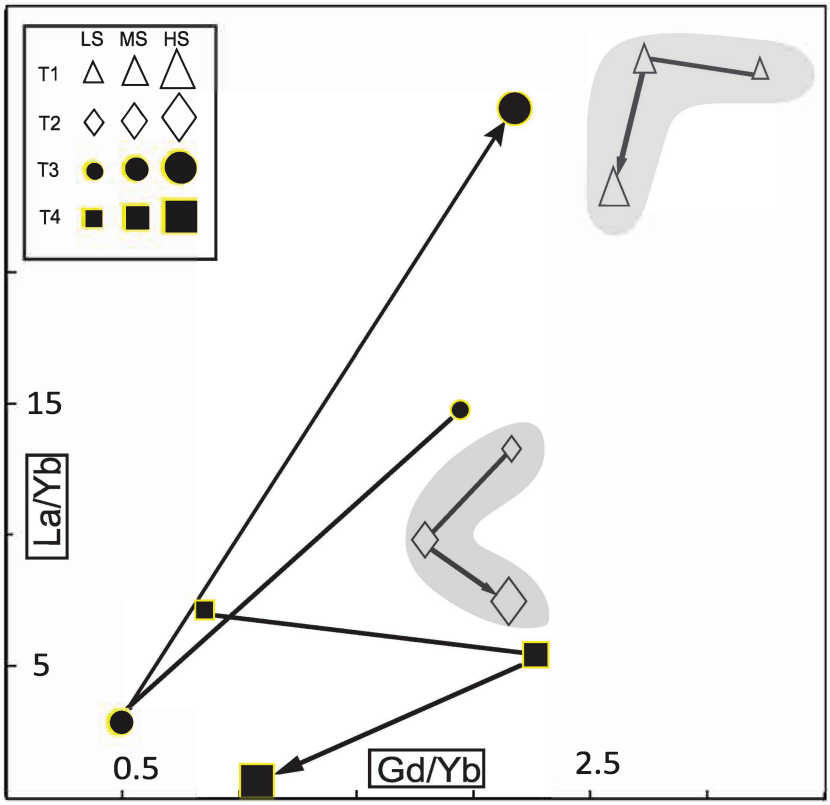

FIGURE 13 | Whole rock REE ratios La/Yb plotted against Gd/Yb for the 4 transects. Transects 1–4 are denoted as T1, T2, T3 and T4. LS, MS and HS denotes low strain, medium strain and high strain, respectively.

direction in shear zones (Brown and Solar 1998). Melt–rock interaction in shear zones has the potential to alter mineral assemblages, leading to hydration and metasomatism in the rock. Remnants of the melt may be preserved as leucosomes, granitic dykes or sills (e.g., Daczko et al. 2016; Stuart, Piazolo, and Daczko 2018; Stuart, Meek, et al. 2018). While all four examined shear zones exhibit evidence of hydration and metasomatism, the distinction between quartz veins observed in the Reynolds Range (T2, Figure 2b) and granitic dykes and lenses observed in the Strangways Range (T4, Figure 2e,f) is indicative of fluid–rock interaction involving aqueous fluid and silicate melt, respectively.

6.2.2 | Petrography and Microstructure

Cordierite and K-feldspar grains within the host granulite facies rocks of T1 (Figure 3a) undergo replacement by muscovite-rich domains (Figure 3b). This alteration is commonly associated with the influx of lower-temperature alkali-bearing aqueous fluid (Ogiermann 2002). Similarly, in T2, K-feldspar grains in augen gneiss exhibit abundant myrmekite development and progressive replacement by mats of fine-grained muscovite (Figures 3e and 6d). These textures spatially associate with fractures and grain boundaries, indicative of hydro-fracturing controlling the extent of the reaction. As anticipated from previous work and field relationships, none of the sheared, medium- to high-strain samples in the Reynolds–Anmatjira Ranges exhibit microstructures indicative of the former presence of melt. These rocks, akin to classic mylonite rocks, display dynamic recrystallisation features, including elongate quartz grains, bending of mica (Figure 5d), a bimodal grain size distribution of quartz (Figure 6e), sutured grain boundaries (Figure 5e), 'core and mantle' structures (Figure 5f) and grains with undulose extinction. Elongation of recrystallised and neocrystallised aggregates of quartz and mica, recrystallised tails and fine-grained foliation anastomosing around deformed relicts are characteristic solid-state flow features (Figure 3; Vernon and Clarke 2008; Daczko & Piazolo, 2022). Myrmekite commonly replaces the margins of K-feldspar grains in deformed felsic rocks, and subsolidus deformation may be a prerequisite for its formation (Vernon 1991). Very heterogeneous strain and local mylonitic zones are also characteristic of solid-state deformation (Passchier and Trouw 2005). Thus, it is convincing that the high-strain rocks from T1 and T2 were formed due to solid-state dynamic recrystallisation.

In contrast, the high-strain samples from the Cattle Water Pass shear zone (T3) present abundant examples of microstructures indicative of the former presence of melt. Plagioclase shows low apparent dihedral angles, commonly between garnet grains (Grt2; Figure 8c) and may form films along grain boundaries (Figure 8c). Plagioclase, K-feldspar and quartz aggregates also display low apparent dihedral angles (Figure 8e). Multiple nearby interstitial and cuspate plagioclase grains display the same petrographic interference colour and extinction angle, suggesting a single interstitial grain connected in three dimensions (Figure 8d). Sillimanite locally replaces plagioclase in finger-like protrusions possibly reflecting dissolution and precipitation that is preferential along one twin orientation of

the plagioclase over the other (Figure 8e inset). Plagioclase is stable in experiments under high pressure if the fluid activity is low, and in the case of dehydration melting experiments, the starting plagioclase should have a grain size $\leq 5\,\mu m$ at 8 kbar (Johannes and Koepke 2001). The grain size of plagioclase from T3 is much greater than $5\,\mu m$, and these display reaction textures within the Cattle Water Pass shear zone. Thus, from the grain size and inferred instability of plagioclase, it is likely that the sillimanite–plagioclase replacement texture indicates an open system, consistent with the ingress of silicate melt. Quartz may also cut K-feldspar in the quartz, K-feldspar and plagioclase mineral associations (Figure 8e). These features, along with numerous neoblasts of garnet in medium strain rocks (Figure 8d), extremely thin and elongate grains of plagioclase along the boundaries of garnet (Figure 8c), 'string of beads' in the low strain rocks of T3 (Figure 8f), and symplectite in all the samples of T4 (Figure 9d,e), strongly suggest the former presence of melt (Holness and Clemens 1999; Clemens and Holness 2000; Holness et al. 2011). Some of these microstructures are overgrown by later phases and show subsequent reaction (e.g., sillimanite replacing plagioclase in Figure 8e), suggesting multiple episodes of silicate melt ingress and egress were likely.

As described above, field evidence such as granitic dykes and biotite selvedges around granitic lenses (Figure 2e,f) supports fluid–rock interaction involving silicate melt in the Gough Dam shear zone (T4; see also Piazolo et al. 2020 and Silva et al. 2022). Yet the samples examined do not show 'classic' microstructures indicative of the former presence of melt akin to those from the Cattlewater Pass shear zone (T3; see also Ghatak et al. 2022). It is probable that the migrating melt escaped before the P–T conditions permitted crystallisation of the quartzo-feldspathic phases (Stuart, Piazolo, and Daczko 2018; Daczko et al. 2016). However, biotite–quartz (Bt–Qz) symplectites in T4 samples exhibit the following features: (1) they replace the rims of granulite facies biotite (Figure 9d,e); (2) occur in proximity to breakdown textures of coarse garnet grains (e.g., sample GTD7-T4-MS Figure 4); and (3) form relatively smaller domains in biotite-dominated samples (e.g., sample GDT4-T4-HS, Figure 4). These textures are common in migmatitic rocks and are considered a late-stage anatectic microstructure where small proportions of melt remain in the migmatite (Sawyer 1999).

Magnetite forms a high proportion of the high-strain sample in T4 (Table 1; Figures S1 and 9c) and replaces sillimanite in places, consistent with high degree fluid–rock interaction. The high proportions of a single mineral (high variance assemblage) possibly indicate the migration and escape of silicate melt via filter pressing, particularly in biotite-rich rocks because of their strong anisotropy (Park and Means 1996). This idea is akin to the crystallisation of an igneous body, wherein the confining pressure created by the first phases on the liquidus forces the interstitial liquid to separate out (Cox et al. 1979). It may explain the absence of microstructures indicative of the former presence of melt in the examined T4 samples, along with some evidence of newly formed quartz pockets within the biotite-rich rocks. Other samples examined from the Gough Dam shear zone in Piazolo et al. (2020) and Silva et al. (2022) show microstructures indicative of the former presence of melt, like equidimensional grains, low apparent angles, films and 'string of beads' textures. The presence of microstructures indicative of the former presence of melt (e.g., samples in T3) permit identification of rocks through which melt has migrated, with some of the melt remaining behind and crystallising, consistent with enrichment in light REE (see next section). In contrast, a lack of melt microstructures in some samples (e.g., samples in T4) is consistent with most of the melt migrating through the rock with little being left behind, possibly leading to a depletion in light REE.

6.2.3 | Major and Trace Element Signatures

The major and trace element patterns within each transect exhibit intricate and highly variable characteristics, aligning with the diverse mineral modes observed in the samples. SiO_2 displays substantial variations across all transects, while Al_2O_3 in T3 and Fe_2O_3 in T4 exhibit consistent patterns of change with increasing strain and metasomatism (Figure 10). The distinctive geochemical disparities among samples within a transect are evident in the mineral assemblage and modes of minerals in each sample (Table 1, Figure S1). For instance, the high-strain (HS) rock in T2 has approximately 30% less silica than the low-strain (LS) homogeneous augen gneiss, accompanied by a rise in MgO from approximately 1% (LS) to about 16% (HS; Table 4). These differences align with changes in mineral modes, wherein a quartzo-feldspathic assemblage in the LS rock is replaced by an assemblage deficient in quartz and enriched in biotite and chlorite (Table 1, Figure S1).

A noticeable divergence is observed in silica behaviour in transects 1 and 2, where silica increases in T1 but decreases in T2. In the presence of a free fluid, the dissolution of a reactant grain at the mineral–fluid interface is driven by the relative solubility of minerals in the fluid (Putnis 2002). Consequently, a mineral will dissolve if a fluid is undersaturated with respect to the solid, resulting in a decrease (as in T2) or increase (as in T1) in the mode of quartz in a rock, respectively (Table 1, Figure S1).

While aluminium is generally considered largely immobile in aqueous fluids during metasomatism, in extreme cases, such as in the presence of partial melts, it can be mobilised, akin to most other elements (Ague 2017). Thus, a silicate melt is suggested as the metasomatic agent in T3 and T4, given the resilience of aluminium to be removed from a rock during aqueous fluid–rock interaction (Middelburg et al. 1988). Trace element patterns between samples of a single transect are remarkably similar for T2 and T3, whereas T1 is relatively enriched and T4 is relatively depleted in trace element content with increasing strain and metasomatism (Figure 11), including Zr and Hf, which are commonly considered immobile. In T1 (Figure S3), the variation of Zr and Hf in the rocks controls the pattern, and this may be explained by a high variation in detrital zircon content in metasedimentary protoliths (Wang et al. 2014). Generally, major element mobility patterns in felsic protoliths across a shear zone reflect information about the source of aqueous fluid and thermobaric conditions during the event (Tursi et al. 2019). However, the complex metasomatic patterns in major and trace elements observed between samples inferred to have undergone aqueous fluid–rock versus silicate melt–rock interaction indicate that larger sample suites and detailed mineral mode data, including accessory minerals, are needed to deconvolute the effects of small-scale protolith mineralogical variation and fluid–rock interaction.

6.2.4 | Rare Earth Element (REE) Signatures

The absolute values of geochemical data can be influenced by rock density; hence, our discussion emphasises patterns and ratios to distinguish T1 and T2 from T3 and T4. Limited rare earth element (REE) metasomatism is implied by the presence of similar systematic REE patterns within T1 and T2 (Figure 12). Both transects cluster together in La/Yb versus Gd/Yb space (Figure 13) and standard deviation of normalised values (~20%–25%) indicates low REE mobility during deformation. In contrast, REE data from samples in T3 and T4 exhibit variability and randomness in terms of REE patterns within the respective transects (Figure 12). The ratios depicted in Figure 13 are more widespread for T3 and T4 compared with T1 and T2, and standard deviations of normalised values (40%–65%) indicate significant REE mobility during deformation in these transects. Notably, the high strain sample from the Gough Dam shear zone (T4) is exceptionally depleted in REE (by three orders of magnitude; red arrow, Figure 12), falling well below chondrite and displaying a highly unusual REE pattern (i.e., shape) with a strong negative Nd anomaly (Figure 12).

Experimental studies by Hermann et al. (2006) and Adam et al. (2014) reveal that partition coefficients of REE are highest in hydrous silicate melts and very low in aqueous fluids. S-type granite melts may selectively scavenge light REE from country rocks, partially explaining their enriched light REE signature (Villaros et al. 2009). Though only based on three samples in a transect, the observation of low REE mobility (T1 and T2, Reynolds–Anmatjira Ranges) compared with higher mobility (T3 and T4, Strangways Range) supports fluid–rock interaction involving aqueous fluid (T1 and T2) versus silicate melt (T3 and T4) (Figure 12). However, caution is needed as there may be some circumstances when aqueous fluids can mobilise REE (e.g., if the fluid is F-rich; Pan and Fleet 1996).

Gresens's analysis plots (Gresens 1967), previously presented for T1 and T2 in Raimondo et al. (2011), reflect the mobility of major elements and volume change across the shear zone. T1 exhibited a volume change of +20%; while for T2, the volume change fell within the range of +15%–37%. In this study, the Gresens analysis plots are available in the supplementary section, where the challenges of utilising such plots for melt-bearing open systems are discussed. The open-system behaviour, involving melt flux through a shear zone, combined with the mobility of nearly all elements in silicate melt, suggests that many elements may be mobile and metasomatised in the case of the Strangways Range shear zones. However, there is a distinct variation in REE mobility across the two cases. REE mobility in aqueous fluid-fluxed systems is low, resulting in systematic patterns within each transect (high correlation coefficient). In contrast, in the melt-fluxed system, REE mobility is high, leading to unsystematic patterns within each transect (low correlation coefficient).

6.3 | Proposed Models

6.3.1 | Syn-Deformational Metasomatism Involving Aqueous Fluid Flux: The Reynolds–Anmatjira Examples

A streamlined three-stage model delineating the hydration of granulite facies rocks in the Reynolds–Anmatjira Ranges and the localisation of strain in shear zones (Figure 14a) integrates microstructural and geochemical insights from T1 and T2. The

TABLE 4 | Whole rock major element data (XRF; oxide weight percent).

Sample		R4	R6	R8	R26	R29	R30	CWP2	CWP3	CWP4	GDT9	GDT7	GDT4
Transect		T1	T1	T1	T2	T2	T2	T3	T3	T3	T4	T4	T4
Degree of strain		LS	MS	HS	LS	MS	HS	LS	MS	HS	LS	MS	HS
SiO_2	(%)	58.84	55.74	70.68	74.21	80.81	41.12	46.63	45.23	45.85	55.69	33.48	31.00
TiO_2	(%)	0.85	0.89	0.51	0.31	0.18	1.85	1.59	0.36	1.16	0.70	3.77	2.19
Al_2O_3	(%)	22.12	24.55	14.74	12.63	10.37	17.86	21.64	24.55	27.85	21.34	15.64	16.24
Fe_2O_3	(%)	6.33	5.26	4.02	2.22	0.96	11.59	15.67	15.18	13.34	7.88	29.74	32.16
Mn_3O_4	(%)	0.03	0.03	0.02	0.03	0.02	0.03	0.22	0.55	0.16	0.04	0.10	0.10
MgO	(%)	4.77	5.04	3.57	0.56	1.01	16.18	4.93	3.60	4.53	2.61	8.21	7.92
CaO	(%)	0.18	0.05	0.02	1.28	0.17	0.14	2.76	7.11	0.45	0.47	0.44	0.01
Na_2O	(%)	1.07	0.54	0.36	2.30	4.68	0.32	2.14	2.16	0.51	3.41	0.18	0.18
K_2O	(%)	5.05	4.49	3.17	5.09	0.55	4.92	4.34	1.62	5.06	6.80	6.79	8.78
P2O5	(%)	0.09	0.04	0.02	0.11	0.07	0.08	0.03	0.06	0.05	0.09	0.04	0.02
L.O.I.	(%)	0.99	3.24	1.96	0.58	0.94	5.60	0.34	0.11	1.15	1.12	0.68	0.57
Total	(%)	100.31	99.87	99.07	99.32	99.74	99.70	100.28	100.52	100.12	100.14	99.06	99.15

Note: R = RAN008 (abbreviated sample prefixes of Raimondo et al. 2011). Transects 1–4 are denoted as T1, T2, T3 and T4. LS, MS and HS denotes low strain, medium strain and high strain, respectively.

model utilises the mineral assemblage changes observed across T2 to elucidate the process of aqueous fluid–rock interaction. Within this transect, the augen gneiss (Qz + Kfs + Pl) undergoes transformation into a predominantly Qz + Ms rock with minor plagioclase. The shear zone may either be newly localised in the granulite facies rocks or reactivated from pre-existing structures.

In Stage 1, the granulite facies precursor exhibits no discernible effects of hydration. Transitioning into Stage 2, the presence of myrmekite indicates the initial modification of the rock through interaction with fluids. Myrmekite nucleation in high strain domains is controlled by pervasive fluid flux (Menegon et al. 2006). Water–rock interaction at the interface between the migrating aqueous fluid and the deforming host rock yields myrmekite and drives reactions that hydrate Qz + Kfs (Figures 14a and 6e), leading to the replacement of these minerals with micaceous mats. Gradually, the fluid infiltrates along grain boundaries and fractures within quartz and plagioclase (Stage 2, Figure 14a; Figure 6d,e). The degree of undulose extinction of quartz grains intensifies in high strain domains compared to low strain domains (Figure 3d,e),

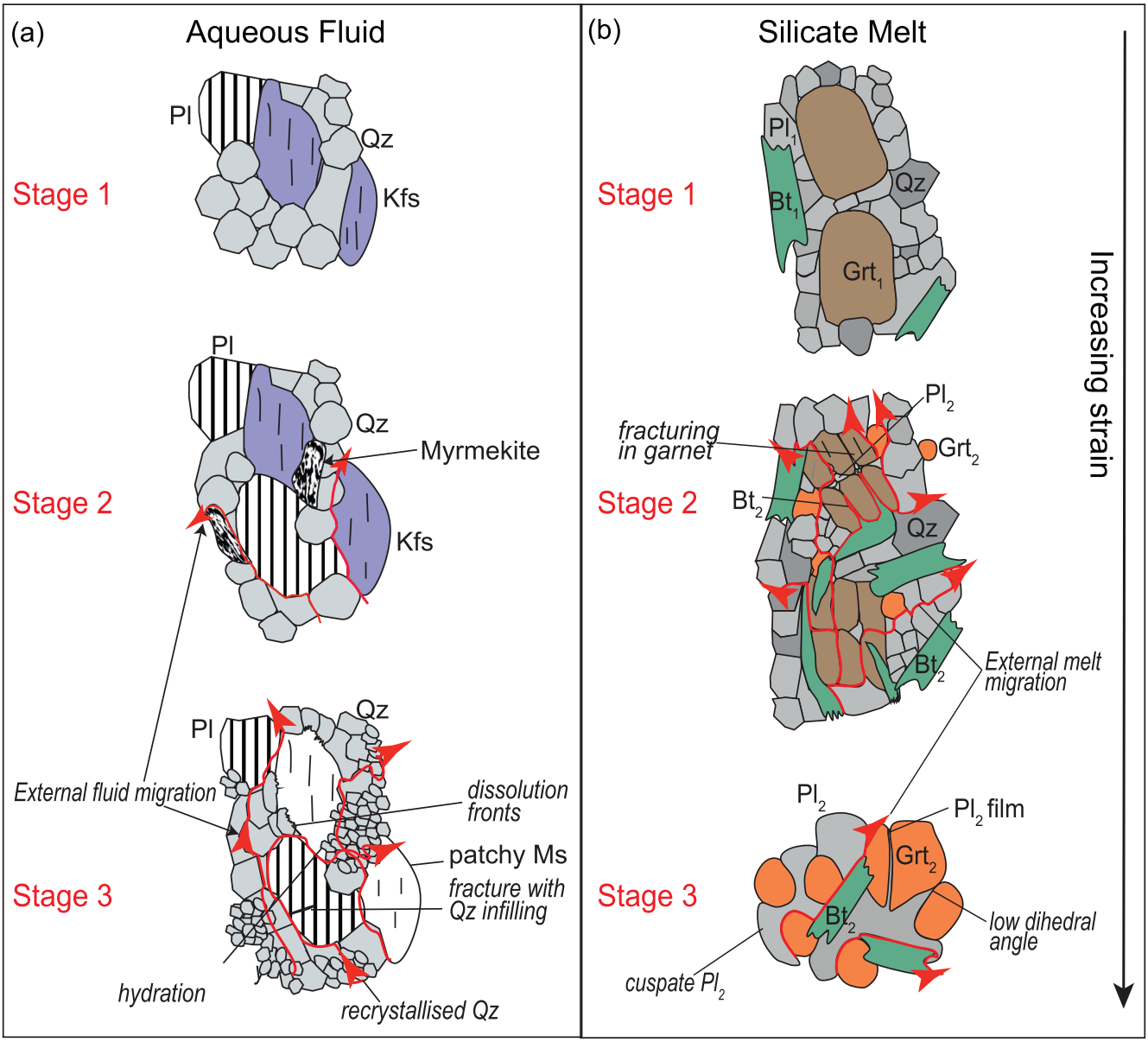

FIGURE 14 | (a) Illustration of the microstructural processes of aqueous fluid infiltration within a shear zone and associated metasomatic changes in the host rock from the Reynolds–Anmatjira Ranges. Stage 2 describes minor changes induced by aqueous fluid infiltration into a low strain rock (Stage 1); Stage 3 denotes the formation of the high strain equivalent (patchy muscovite, dissolution fronts, recrystallised quartz grains) due to syn-deformational fluid–rock interaction. (b) Illustration of the microstructural processes of melt infiltration and melt–rock reaction within a shear zone and associated metasomatic changes in the host rocks from the Strangways Range. Stage 1 shows the early stage of melt infiltration with minor modification of the host rock; Stage 2 shows melt–rock interaction by the formation of neoblasts of garnet at the expense of older garnet grains (Grt1), while in Stage 3, significant modification of the protolith rock is shown by high modes of coarse garnet, biotite and plagioclase with less evident foliation. Note that quartz is consumed between stages 2 and 3. Also, upon cooling, melt freezes preserving grains subtending low apparent dihedral angles, forming films between grains and cuspate grain shapes, particularly for the new plagioclase grains (Pl_2).

accompanying the development of a bimodal grain size distribution (Stage 3, Figure 14a; Figure 6e,f). This is attributed to the recrystallisation of quartz, resulting in an overall reduction in grain size and the formation of elongate quartz domains and grains (Stage 3, Figure 14a; Figure 3). High strain domains may also exhibit distinctive shear sense indicators such as mica fish, asymmetrical distribution of recrystallised quartz and tailed feldspar porphyroclasts (Figures 3e,f and 6c), contingent on the extent of mylonitisation. The preservation of these features implies recrystallisation and dissolution processes during progressive deformation (Ten Grotenhuis et al. 2003).

Ultimately, the host rock undergoes substantial replacement by a metasomatised assemblage of micaceous phases (Stage 3, Figures 14a and 6c). Aqueous fluid-induced hydration can significantly alter the rheology of the shear zone (Maggi et al. 2014), given the deformation geometry and favourable mineral orientations. The substitution of robust framework silicates with weaker phyllosilicates, accompanied by volume reduction during phyllosilicate formation, enhances reaction weakening and facilitates increased fluid flow within the system. In such a fluid-fluxed system, phyllosilicates with a strong shape preferred orientation and contiguities can substantially weaken the crust (Wintsch et al. 1995).

Most shear zone arrays evolve as self-organised deformation systems with interconnected shear networks. Once matured, the kinematic and mechanical behaviour of the shear zone is shaped by the rheological properties of the interconnected shear network (Gardner et al. 2017; Holdsworth et al. 2001). Consequently, these hydration mechanisms can exert significant control on the crustal dynamics of a large terrain over considerable geological time.

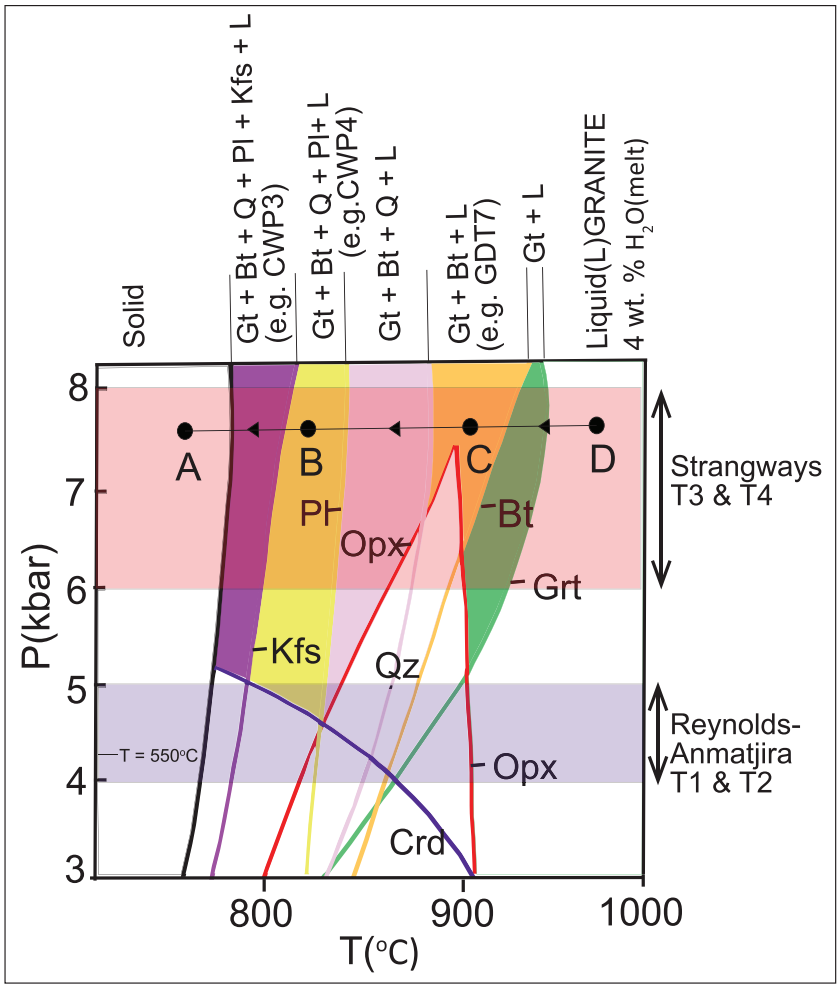

FIGURE 15 | Pressure–temperature phase diagram for a S-type granitic composition with 4 wt. % H_2O in the melt (Clemens and Wall 1981). The pressure ranges of the shear zones in Strangways Range and the Reynolds–Anmatjira Ranges are denoted by the red band (6–8 kbar) and blue band (4–5 kbar), respectively. The black dots with arrows show the progressive crystallisation of minerals predicted upon cooling at pressures comparable to those experienced by rocks in T3 and T4 due to migration of melt through these shear zones. In this example at 7.5 kbar, a granite liquid (D) will first crystallise garnet and then garnet–biotite (C) and at lower T. Quartz, plagioclase (B) and finally K-feldspar will progressively crystallise with cooling until the magma reaches the solidus (A). If a granite melt fluxes a shear zone at ~900°C (point C), the silicate liquid will precipitate garnet and biotite, while at the same time dissolving quartz, plagioclase and K-feldspar. These relationships may produce a rock similar to GDT7-T4-MS, for example. Mineral abbreviations: Qz, quartz; Kfs, K-feldspar; Pl, plagioclase; Crd, cordierite; Bt, biotite; Grt, garnet; Opx, orthopyroxene.

6.3.2 | Syn-Deformational Metasomatism Involving Silicate Melt Flux: The Strangways Range Examples

A condensed three-stage model depicting the hydration of granulite facies rocks in the Strangways Range and the localisation of strain in shear zones (Figure 14b) integrates field- and microstructural-scale observations from T3 and T4. The estimated pressure–temperature (P–T) conditions for these shear zones range from 600°C to 660°C and from 6 to 7 kbar (Balle'vre et al. 2000; Bendall 2000; Silva et al. 2022). Leveraging the comprehensive microstructures observed in T3, which offer greater preservation, the model conceptualises the melt–rock interaction process, supplementing previous descriptions of different samples from the Gough Dam shear zone (T4) by Piazolo et al. (2020) and Silva et al. (2022). In T3, garnet gneiss (Qz + Pl + Grt + Bt) transforms into a dominantly Pl–Grt–Bt–rich rock.

Stage 1 illustrates the precursor granulite facies rock with coarse garnet, quartz, plagioclase and a few biotite grains. As strain intensifies in Stage 2, shearing of the granulite facies rocks channels melt into these zones, either migrating as dykes or through deformation-assisted diffuse porous flow (e.g., Stuart, Meek, et al. 2018b). In melt-present systems, the solubility of minerals is primarily governed by the melt composition and temperature. At very high temperatures (above the liquidus temperature of the melt), all minerals tend to dissolve into the melt. Therefore, melt–rock interaction at the interface between the migrating melt and the deforming host rock prompts reactions dissolving minerals not stable in the melt, while other minerals may crystallise from the melt at lower temperatures (e.g., Daczko et al. 2016). The proportions of dissolution and crystallisation hinge on the composition and temperature of the system. This dynamic version of hydration–crystallisation reactions (Beard et al. 2004) leads to the dissolution of precursor rock and precipitation of a biotite-rich assemblage in equilibrium with the fluxing melt (Stuart, Meek, et al. 2018b; Meek et al. 2019). These reactions initiate along grain boundaries or fractures within grains (e.g., plagioclase and biotite replacing garnet; Stage 2, Figures 14b and 8b) and at the margins of larger melt components (e.g., in a selvedge adjacent to leucosome dykes or lenses; red arrow, Figure 14b; Figure 2e,f).

In Stage 2, the host rock undergoes substantial replacement by a new mineral assemblage, dictated by the composition and temperature of the fluxing melt. The shear zone may also contain partially reacted granulite relicts and variably deformed leucosome dykes (e.g., Figure 2e) and lenses (e.g., Figure 2f). Microstructures indicative of the former presence of melt are preserved once the shear zone drops below the solidus, and any remaining melt crystallises. These include quartz–K-feldspar–plagioclase aggregates, microgranitoid inclusions, plagioclase films, cuspate plagioclase and felsic minerals with low apparent dihedral angles (Stage 3, Figure 14b; Figure 8a,c,d,f).

The origin of granitic melts inferred to have fluxed shear zones in the Strangways Range is traced back to the adjacent Harts Range. Abundant evidence of partial melting in sedimentary and volcanic rocks before and during the Alice Springs Orogeny (Buick et al. 2008; Maidment et al. 2013; Tucker et al. 2015) supports this proposition. Partial melts of sedimentary rocks contain 4–6 wt. % water (White et al. 2001), and experimental studies on such granites (e.g., Clemens and Wall 1981) indicate equilibration with different assemblages during melt–rock interaction in a shear zone. For example, a high-T granitic melt near

TABLE 5 | Toolbox for distinguishing between aqueous fluid and silicate melt in hydration of protolith rocks in a shear zone.

Technique	Effective in differentiating between aqueous fluid and silicate melt interaction in high strain zones	Aqueous fluid	Silicate melt
Field relationship	Yes	Quartz veins, subsolidus mineral assemblage of hydrated rocks (chlorite and andalusite)	Dykes, pegmatites, leucosome lenses, supra-solidus mineral assemblage of hydrated rocks (K-feldspar, sillimanite and garnet)
Mineral assemblage, textures and microstructure	Yes	Reduction in assemblage variance. Absence of microstructures indicative of the former presence of melt. Presence of mylonitic textures (e.g., asymmetric recrystallised quartz, bimodal grain size, highly undulose quartz grains)	Reduction in assemblage variance. Microstructures indicative of the former presence of melt (e.g., films along grain boundaries, low dihedral angles, felsic veins, string of beads texture, Pl-Qtz-Kfs mineral association)
Major and trace element analyses	No	No significant distinguishing pattern	No significant distinguishing pattern
Rare earth element analysis	Yes	Systematic patterns and less mobility of elements	Random patterns indicating much higher mobility of elements

its liquidus (point C, Figure 15) may dissolve most minerals in a pre-existing rock assemblage, only crystallising garnet ± biotite (near-liquidus phases) as it fluxes through a shear zone. This melt–rock interaction yields rocks like the uppermost part of CWP4-T3-HS or sample GDT7-T4-MS, rich in biotite and garnet and poor in quartzo-feldspathic minerals (Figure 4). In contrast, a medium-T granitic melt may also crystallise quartz ± plagioclase (point B, Figure 15), resulting in rocks like CWP-T3-MS rich in garnet, biotite, plagioclase ± quartz. The model emphasises the dominance of melt properties influencing key reactions and crystallisation products (Figure 15). The absence of orthopyroxene in the studied shear zones aligns with pressures above ~7 kbar (Figure 15). The presence of aluminous minerals, including biotite, garnet and sillimanite, reflects an S-type granitic liquid sourced from the partial melting of metasedimentary rocks (e.g., Craven and Daczko 2018), akin to those in the Harts Range Group. Figure 15 also underscores the melt's capacity to dissolve pre-existing minerals into the melt, allowing these components to be transported to structurally higher levels, significantly reducing their mode in the resulting deeper level rocks. The higher temperature conditions during melt–rock interaction (point C, Figure 15) result in a higher variance assemblage, characteristic of metasomatic processes (Yardley 2009).

A similar model has been proposed for mafic systems where granulite facies lower crust is fluxed by gabbroic melts in the roots of magmatic arcs (Daczko et al. 2016; Stuart, Piazolo, and Daczko 2018; Stuart, Meek, et al. 2018; Meek et al. 2019). In these systems, two-pyroxene–hornblende granulites are replaced by high-variance assemblages, including hornblendite, clinozoisite hornblendite and garnetite. Examining low to high strain samples, as done in this study, illustrates the progressive replacement of pre-existing minerals (pyroxene and plagioclase) predominantly by hornblende in these mafic systems. The substantial reductions in plagioclase mode identified during melt–rock interaction in the arc lower crust underscore the solubility of plagioclase into the mafic melts as they traverse the crust (Daczko et al. 2016). This process, occurring at high temperatures (near the liquidus and above plagioclase stability), is highly analogous to the solubility of quartz and plagioclase in high-temperature granitic melts inferred in this study. Interestingly, REE mobility during melt–rock interaction in the arc lower crust has also been recognised (Stuart, Meek, et al. 2018; Meek et al. 2019).

Considering a similar melt flux scenario at lower pressure suitable for the shear zones in the Reynolds–Anmatjira Ranges (blue band, Figure 15), the model's mineral assemblage (Opx, Grt, Kfs, Crd) does not resemble the observed mineral assemblages (e.g., chlorite-bearing) from T1 and T2. This observation substantiates field, microstructural and geochemical arguments for syn-deformational metasomatism driven by aqueous fluid flux in that area.

7 | Conclusion: A Toolbox for Identifying Hydration in Shear Zones by Aqueous Fluid Versus Silicate Melt

The pivotal findings of this study are succinctly presented in Table 5, offering a comprehensive toolset and emphasising the range of data required to facilitate the interpretation of hydrated shear zones in terms of metasomatic agents or fluid types. Firstly, it is highlighted that rocks in hydrated shear zones commonly exhibit veins, dykes and/or leucosomes, each hosting mineral assemblages that enable inference of the fluid type from which they crystallised. Establishing the metamorphic grade becomes imperative to discern whether deformation transpired at subsolidus or supra-solidus conditions. Additionally, emphasis is placed on meticulously considering the temporal relationship between veins and dykes and the high-strain deformation event.

Secondly, the identification of preserved microstructures indicative of the former presence of melt emerges as robust evidence signalling supra-solidus conditions and deformation in the presence of melt. Thirdly, it is underscored that while major and trace element analysis successfully identifies metasomatism, it does not sufficiently discriminate between aqueous fluid and silicate melt as the metasomatic agent. Instead, modification of rare earth element patterns (i.e., shape) is emphasised as a promising geochemical indicator for distinguishing between hydration in shear zones induced by aqueous fluid (resulting in minor modification of patterns) and silicate melt (associated with moderate to extreme modification of patterns).

Acknowledgements

ARC Discovery Project funding (DP160103449) to T.R. and N.R.D. provided financial support to conduct this research. David Silva is thanked for initial processing and powdering of the samples. Reviews by Ake Fagereng and the editor, and editorial handling by Katherine Evans greatly improved this manuscript. Open access publishing facilitated by Macquarie University, as part of the Wiley - Macquarie University agreement via the Council of Australian University Librarians.

Conflicts of Interest

The authors declare no conflicts of interest.

Data Availability Statement

The data that support the findings of this study are available from the corresponding author upon reasonable request.

References

Adam, J., M. Locmelis, J. C. Afonso, T. Rushmer, and M. Fiorentini. 2014. "The Capacity of Hydrous Fluids to Transport and Fractionate Incompatible Elements and Metals Within the Earth's Mantle." *Geochemistry, Geophysics, Geosystems* 15: 2241–2253. https://doi.org/10.1002/2013GC005199.

Ague, J. J. 2017. "Element Mobility During Regional Metamorphism in Crustal and Subduction Zone Environments With a Focus on the Rare Earth Elements (REE)." *American Mineralogist* 102, no. 9: 1796–1821.

Asimus, J. L., N. R. Daczko, and I. S. Ezad. 2023. "Melt-Present Deformation at the Entia Dome, Central Australia: A Metamorphic Core Complex Formed During Lower Crustal Tectonic Extrusion." *Lithos* 448: 107170.

Ballevre, M., B. J. Hensen, and B. Reynard. 1997. "Orthopyroxene-Andalusite Symplectites Replacing Cordierite in Granulites From the Strangways Range (Arunta Block, Central Australia): A New Twist to the Pressure-Temperature History." *Geology* 25: 215–218.

Balle'vre, M., A. Moller, and B. Hensen. 2000. "Exhumation of the Lower Crust During Crustal Shortening: An Alice Springs (380 Ma) Age for a Prograde Amphibolite Facies Shear Zone in the Strangways

Metamorphic Complex (Central Australia)." *Journal of Metamorphic Geology* 18: 737–747.

Beard, J. S., P. C. Ragaland, and T. Rushmer. 2004. "Hydration Crystallization Reactions Between Anhydrous Minerals and Hydrous Melt to Yield Amphibole and Biotite in Igneous Rocks: Description and Implications." *Journal of Geology* 112, no. 5: 617–621.

Bendall, B. 2000. *Mid-Palaeozoic Shear Zones in the Strangways Range: A Record of Intracratonic Tectonism in the Arunta Inlier, Central Australia*. Unpublished PhD Thesis submitted to. University of Adelaide, Faculty of Science.

Bons, P. 2001. "The Formation of Large Quartz Veins by Rapid Ascent of Fluids in Mobile Hydrofractures." *Tectonophysics* 336, no. 1: 1–17.

Bouchez, J. L., C. Delas, G. Gleizes, A. Nédélec, and M. Cuney. 1992. "Submagmatic Microfractures in Granites." *Geology* 20, no. 1: 35–38.

Brown, M. 1994. "The Generation, Segregation, Ascent and Emplacement of Granite Magma: The Migmatite-to-Crustally-Derived Granite Connection in Thickened Orogens." *Earth-Science Reviews* 36, no. 1–2: 83–130.

Brown, M., and G. Solar. 1998. "Shear-Zone Systems and Melts: Feedback Relations and Self-Organization in OROGENIC Belts." *Journal of Structural Geology* 20, no. 2–3: 211–227.

Buick, I., A. Storkey, and I. Williams. 2008. "Timing Relationships Between Pegmatite Emplacement, Metamorphism and Deformation During the Intra-Plate Alice Springs Orogeny, Central Australia." *Journal of Metamorphic Petrology* 26, no. 9: 915–936.

Busch, W.. 1974. "Initial Melting at Grain Boundaries. Part II: Melting of Rocks of Granodioritic, Quartzdioritic and Tonalitic Composition." *Neues Jahrbuch für Mineralogie – Monatshefte* 8: 345–370.

Candela, P., and H. Holland. 1983. "The Partitioning of Copper and Molydenum Between Silicate Melts and Aqueous Fluids." *Geochimica et Cosmochimica Acta* 4, no. 2: 373–380.

Cartwright, I., I. Buick, D. Foster, and D. Lambert. 1999. "Alice Springs Age Shear Zones From the South Eastern Reynolds Range, Central Australia." *Australian Journal of Earth Sciences* 46: 355–363.

Clarke, G., R. White, S. Lui, J. Fitzherbert, and N. Pearson. 2007. "Contrasting Behaviour of Rare Earth and Major Elements During Partial Melting in Granulite Facies Migmatites, Wuluma Hills, Arunta Block, Central Australia." *Journal of Metamorphic Geology* 25: 1–18.

Clemens, J., and M. Holness. 2000. "Textural Evolution and Partial Melting of Arkose in a Contact Aureole: A Case Study and Implications." *Visual Geosciences* 5: 1–14.

Clemens, J. D., and V. J. Wall. 1981. "Origin and Crystallization of Some Peraluminous (S-type)." *Canadian Mineralogist* 19, no. 1: 111–131.

Collins, W., and C. Teyssier. 1989. "Crustal Scale Ductile Fault Systems in the Arunta Inlier, Central Australia." *Tectonophysics* 158, no. 1: 49,60,63–58,60,66.

Cox, K. G., J. D. Bell, and R. J. Pankhurst. 1979. *The Interpretation of Igneous Rocks*. Springer. https://doi.org/10.1007/978-94-017-3373-1.

Craven, S. J., and N. R. Daczko. 2018. "High Temperature-Low-Pressure Metamorphism and the Production of S-Type Granites of the Hillgrove Supersuite, Southern New England Orogen, NSW, Australia." *Australian Journal of Earth Sciences* 65, no. 2: 191–207.

Daczko, N., S. Piazolo, U. Meek, C. Stuart, and V. Elliott. 2016. "Hornblendite Delineates Zones of Mass Transfer Through the Lower Crust." *Scientific Reports* 6: 1–6.

Daczko, N. R., and S. Piazolo. 2022. "Recognition of Melferite–A Rock Formed in Syn-Deformational High-Strain Melt-Transfer Zones Through Sub-Solidus Rocks: A Review and Synthesis of Microstructural Criteria." *Lithos* 430: 106850.

Essaifi, A., R. Capdevila, S. Fourcade, J. L. Lagarde, M. Ballèvre, and C. H. Marignac. 2004. "Hydrothermal Alteration, Fluid Flow and Volume Change in Shear Zones: The Layered Mafic–Ultramafic Kettara Intrusion (Jebilet Massif, Variscan Belt, Morocco)." *Journal of Metamorphic Geology* 22, no. 1: 25–43.

Etheridge, M. A., N. R. Daczko, T. Chapman, and C. A. Stuart. 2021. "Mechanisms of Melt Extraction During Lower Crustal Partial Melting." *Journal of Metamorphic Geology* 39, no. 1: 57–75.

Finch, M. A., R. F. Weinberg, and N. J. Hunter. 2016. "Water Loss and the Origin of Thick Ultramylonites." *Geology* 44, no. 8: 599–602.

Gapais, D., and S. White. 1982. "Ductile Shear Bands in Naturally Deformed Quartzite." *Textures and Microstructures* 5, no. 1: 1–17.

Gardner, R., S. Piazolo, L. Evans, and N. R. Daczko. 2017. "Patterns of Strain Localization in Heterogeneous, Polycrystalline Rocks–A Numerical Perspective." *Earth and Planetary Science Letters* 463: 253–265.

Gardner, R. L., N. R. Daczko, S. Piazolo, J. Adam, and U. Meek. 2025. "Melt–Rock Interaction Experiments Reveal Rapid Microstructural and Chemical Changes at Lower Crustal Conditions." *Journal of Metamorphic Geology* 43: 341–358.

Ghatak, H., R. L. Gardner, N. R. Daczko, S. Piazolo, and L. Milan. 2022. "Oxide Enrichment by Syntectonic Melt-Rock Interaction." *Lithos* 414: 106617.

Glassley, W. E., L. J. Crossey, and I. P. Montañez. 2016. "Fluid–Rock Interaction." In *Encyclopedia of Geochemistry*, 1–4. Springer.

Gresens, R. 1967. "Composition-Volume Relationships of Metasomatism." *Chemical Geology* 2: 47–55.

Griffin, W. L., W. J. Powell, N. J. Pearson, and S. Y. O'Reilly. 2008. "GLITTER: Data Reduction Software for Laser Ablation ICP-MS." In *Laser Ablation-ICP-MS in the Earth Sciences*, Mineralogical Association of Canada Short Course Series, edited by P. Sylvester, Vol. 40, 204–207.

Hand, M., and I. Buick. 2001. *Tectonic Evolution of the Reynolds-Anmatjira Ranges: A Case Study in Terrain Reworking From the Arunta Inlier, Central Australia*. Vol. 184, 237–260. Geological Society of London, Special Publications.

Hasalova, P., K. Schulmann, O. Lexa, et al. 2008. "Origin of Migmatites by Deformation-Enhanced Melt Infiltration: A New Model Based on Quantitative Microstructural Analysis." *Journal of Metamorphic Geology* 26: 29–53.

Hedenquist, J. W., and J. B. Lowenstern. 1994. "The Role of Magmas in the Formation of Hydrothermal Ore Deposits." *Nature* 370, no. 6490: 519–527.

Hermann, J., C. Spandler, A. Hack, and A. Korsakov. 2006. "Aqueous Fluids and Hydrous Melts in High-Pressure and Ultra-High Pressure Rocks: Implications for Element Transfer in Subduction Zones." *Lithos* 92, no. 3–4: 399–417.

Holdsworth, R., M. Stewart, J. Imber, and R. Strachan. 2001. "The Structure and Rheological Evolution of Reactivated Continental Fault Zones: A Review and Case Study." *Geological Society, London, Special Publications* 184, no. 1: 115. https://doi.org/10.1144/GSL.SP.2001.184.01.07.

Holness, M., and J. Clemens. 1999. "Partial Melting of the Appin Quartzite Driven by Fracture-Controlled H_2O Infiltration in the Aureole of the Ballachulish Igneous Complex, Scottish Highlands." *Contributions to Mineralogy and Petrology* 136: 154–168.

Holness, M., B. Cesare, and E. Sawyer. 2011. "Melted Rocks Under the Microscope: Microstructures and Their Interpretation." *Elements* 7: 247–252.

Holyoke, C., and J. Tullis. 2006. "The Interaction Between Reaction and Deformation: An Experimental Study Using a Biotite + Plagioclase + Quartz Gneiss." *Journal of Metamorphic Petrology* 24, no. 8: 743–762.

Iyer, K., B. Jamtveit, J. Mathiesen, A. Malthe-Sørenssen, and J. Feder. 2008. "Reaction-Assisted Hierarchical Fracturing During Serpentinization." *Earth and Planetary Science Letters* 267, no. 3–4: 503–516.

Jefferies, S., R. E. Holdsworth, C. Wibberley, T. Shimamoto, and C. J. Spiers. 2006. "The Nature and Importance of Phyllonite Development in Crustal-Scale Fault." *Journal of Structural Geology* 28, no. 2: 220–235.

Johannes, W., and J. Koepke. 2001. "Incomplete Reaction of Plagioclase in Experimental Dehydration Melting of Amphibolite." *Australian Journal of Science* 48: 581–590.

Korzhinskiĭ, D. S. 1959. *Physicochemical Basis of the Analysis of the Paragenesis of Minerals*. Consultants Bureau.

Lister, G. L., and A. W. Snoke. 1984. "SC Mylonites." *Journal of Structural Geology* 6, no. 6: 617–638.

Losh, S. 1989. "Fluid-Rock Interaction in an Evolving Ductile Shear Zone and Across the Brittle-Ductile Transition, Central Pyrenees, France." *American Journal of Science* 289: 600–648.

Maggi, M., F. Rossetti, G. Ranalli, and T. Theye. 2014. "Feedback Between Fluid Infiltration and Rheology Along a Regional Ductile-to-Brittle Shear Zone: The East Tenda Shear Zone (Alpine Corsica)." *Tectonics* 33, no. 3: 253–280. https://doi.org/10.1002/2013TC003370.

Maidment, D. W., M. Hand, and I. S. Williams. 2013. "High Grade Metamorphism of Sedimentary Rocks During Palaeozoic Rift Basin Formation in Central Australia." *Gondwana Research* 24, no. 3–4: 865–885.

McDonough, W., and S. Sun. 1995. "The Composition of the Earth." *Chemical Geology* 120, no. 3–4: 223–253.

Meek, U., S. Piazolo, and N. R. Daczko. 2019. "The Field and Microstructural Signatures of Deformation-Assisted Melt Transfer: Insights From Magmatic Arc Lower Crust, New Zealand." *Journal of Metamorphic Geology* 37, no. 6: 795–821.

Mehnert, K. R., W. Busch, and G. Schneider. 1973. "Initial Melting at Grain Boundaries of Quartz and Feldspar in Gneisses and Granulites." *Neues Jahrbuch für Mineralogie – Monatshefte* 1973, no. 4: 165–183.

Menegon, L., G. Pennacchioni, and H. Stünitz. 2006. "Nucleation and Growth of Myrmekite During Ductile Shear Deformation in Metagranites." *Journal of Metamorphic Geology* 24, no. 7: 553–568.

Middelburg, J., H. Cornelis, and J. Woittiez. 1988. "Chemical Processes Affecting the Mobility of Major, Minor and Trace Elements During Weathering of Granitic Rocks." *Chemical Geology* 68, no. 3–4: 253–273.

Milke, R., G. Neusser, K. Kolzer, and B. Wunder. 2013. "Very Little Water Is Necessary to Make a Dry Solid Silicate System Wet." *Geology* 41, no. 2: 247–250.

Mohanty, S., and J. Ramsay. 1994. "Strain Partitioning in Ductile Shear Zones: An Example From a Lower Pennine Nappe of Switzerland." *Journal of Structural Geology* 16, no. 5: 663–676.

Newton, R. 1990. "Fluids and Shear Zones in the Deep Crust." *Tectonophysics* 182, no. 1–2: 21–37.

Norman, A. (1991). Unpublished PhD Thesis. *The Structural and Metamorphic Evolution of the Central Arunta Block: Evidence From the Strangways Metamorphic Complex and the Harts Range Group, Central Australia. Submitted to the School of Earth Sciences*, 13. N.S.W. 2109, Australia: Macquarie University.

Ogiermann, J. 2002. *Cordierite and Its Retrograde Breakdown Products as Monitors of Fluid-Rock Interaction During Retrograde Path Metamorphism: Case Studies in the Schwarzwald and the Bayerische Wald (Variscan Belt, Germany)*. Unpub. Doctoral Thesis submitted to. Germany: Combined Faculties for the Natural Sciences and for Mathematics of the Ruperto-Carola University of Heidelberg.

Pan, Y., and M. E. Fleet. 1996. "Rare Earth Element Mobility During Prograde Granulite facies Metamorphism: Significance of Fluorine." *Contributions to Mineralogy and Petrology* 123, no. 3: 251–262.

Park, Y., and W. Means. 1996. "Direct Observation of Deformation Processes in Crystal Mushes." *Journal of Structural Geology* 18, no. 6: 847–858.

Passchier, C., and C. Simpson. 1986. "Porphyroclast Systems as Kinematic Indicators." *Journal of Structural Geology* 8, no. 8: 831–843.

Passchier, C. W., and R. A. Trouw. 2005. *MICROTECTONICS*. Springer Science & Business Media.

Piazolo, S., N. R. Daczko, D. Silva, and T. Raimondo. 2020. "Melt-Present Shear Zones Enable Intracontinental Orogenesis." *Geology* 48, no. 7: 643–648.

Putnis, A. 2002. "Mineral Replacement Reactions: From Macroscopic Observations to Microscopic Mechanisms." *Mineralogical Magazine* 66, no. 5: 689–708.

Raimondo, T., C. Clark, M. Hand, and K. Faure. 2011. "Assessing the Geochemical and Tectonic Impacts of Fluid–Rock Interaction in Mid-Crustal Shear Zones: A Case Study From the Intracontinental Alice Springs Orogen, Central Australia." *Journal of Metamorphic Geology* 29: 821–850.

Raimondo, T., C. Clark, M. Hand, J. Cliff, and C. Harris. 2012. "High-Resolution Geochemical Record of Fluid–Rock Interaction in a Mid-Crustal Shear Zone: A Comparative Study of Major Element and Oxygen Isotope Transport in Garnet." *Journal of Metamorphic Geology* 30, no. 3: 255–280.

Raimondo, T., M. Hand, and W. Collins. 2014. "Compressional Intracontinental Orogens: Ancient and Modern Perspectives." *Earth-Science Reviews* 130: 128–153.

Ramsay, J., R. Lisle, and M. Huber. 1983. *The Techniques of Modern Structural Geology*. Academic Press.

Rutter, E. H., and D. H. K. Neumann. 1995. "Experimental Deformation of Partially Molten Westerly Granite Under Fluid-Absent Conditions, With Implications for the Extraction of Granitic Magmas." *Journal of Geophysical Research: Solid Earth* 100 no. B8: 15697–15715.

Sawyer, E. W. 1999. "Criteria for the Recognition of Partial Melting." *Physics and Chemistry of the Earth, Part A: Solid Earth and Geodesy* 24, no. 3: 269–279.

Sawyer, E. W., and M. Brown. 2008. *Working With Migmatites*. Mineralogical Association of Canada.

Scrimgeour, I. R., and M. Ahmad. 2013. "Chapter 2: Geological Framework." In *Geology and Mineral Resources of the Northern Territory (Vol. Special Publication 5)*, edited by T. J. Munson and M. Ahmad. Northern Territory Geological Survey.

Silva, D., N. R. Daczko, S. Piazolo, and T. Raimondo. 2022. "Glimmerite: A Product of Melt-Rock Interaction Within a Crustal-Scale High-Strain Zone." *Gondwana Research* 105: 160–184.

Silva, D., S. Piazolo, N. R. Daczko, G. Houseman, T. Raimondo, and L. Evans. 2018. "Intracontinental Orogeny Enhanced by Far-Field Extension and Local Weak Crust." *Tectonics* 37, no. 12: 4421–4443.

Stenvall, C. A., A. Fagereng, J. F. A. Diener, C. Harris, and P. E. Janney. 2020. "Sources and Effects of Fluids in Continental Retrograde Shear Zones: Insights From the Kuckaus Mylonite Zone, Namibia." *Geofluids* 2020, no. 1: 3023268.

Stuart, C., S. Piazolo, and N. Daczko. 2016. "Mass Transfer in the Lower Crust: Evidence for Incipient Melt Assisted Flow Along Grain Boundaries in the Deep Arc Granulites of Fiordland, New Zealand." *Geochemistry, Geophysics, Geosystems* 17: 3733–3753. https://doi.org/10.1002/2015GC006236.

Stuart, C., N. Daczko, and S. Piazolo. 2017. "Local Partial Melting of the Lower Crust Triggered by Hydration Through Melt-Rock Interaction: An Example From Fiordland, New Zealand." *Journal of Metamorphic Petrology* 35: 213–230.

Stuart, C. A., U. Meek, N. Daczko, S. Piazolo, and J. Huang. 2018. "Chemical Signatures of Melt–Rock Interaction in the Root of a Magmatic Arc." *Journal of Petrology* 59, no. 2: 321–340.

Stuart, C. A., S. Piazolo, and N. Daczko. 2018. "The Recognition of Former Melt Flux Through High-Strain Zones." *Journal of Metamorphic Geology* 36, no. 8: 1049–1069.

Ten Grotenhuis, S., R. A. J. Trouw, and C. W. Passchier. 2003. "Evolution of Mica Fish in Mylonitic Rocks." *Tectonophysics* 372, no. 1–2: 1–21. https://doi.org/10.1016/S0040-1951(03)00231-2.

Tetley, M. G., and N. R. Daczko. 2014. "Virtual Petrographic Microscope: A Multi-Platform Education and Research Software Tool to Analyse Rock Thin Sections." *Australian Journal of Earth Sciences* 61: 631–637.

Tommasi, A., A. Langone, J. A. Padron-Navarta, A. Zanetti, and A. Vauchez. 2017. "Hydrous Melts Weaken the Mantle, Crystallization of Pargasite and Phlogopite Does Not: Insights From a Petrostructural Study of the Finero Peridotites, Southern Alps." *Earth and Planetary Science Letters* 477: 59–72.

Touret, J. L., and J.-M. Huizenga. 2011. "Fluids in Granulites." *Geological Society of America Memoirs* 207: 25–37.

Tucker, N. M., M. Hand, and J. L. Payne. 2015. "A Rift-Related Origin for Regional Medium-Pressure, High-Temperature Metamorphism." *Earth and Planetary Science Letters* 421: 75–88.

Tursi, F., V. Festa, A. Fornelli, F. Micheletti, and R. Spiess. 2019. "Syn-Shearing Mobility of Major Elements in Ductile Shear Zones: State of the Art for Felsic Deformed Protoliths." *Periodico di Mineralogia* 87, no. 3: 289–308.

Van der Molen, I., and M. Paterson. 1979. "Experimental Deformation of Partially-Melted Granite." *Contributions to Mineralogy and Petrology* 70: 299–318.

Vernon, R. 1991. "Questions About Myrmekite in Deformed Rocks." *Journal of Structural Geology* 13, no. 9: 979–985.

Vernon, R. H. 2000. "Review of Microstructural Evidence of Magmatic and Solid-State Flow." *Visual Geosciences* 5, no. 2: 1–23.

Vernon, R. H. 2011. "Microstructures of Melt-Bearing Metamorphic Rocks." In *Origin and Evolution of Precambrian High-Grade Gneiss Terrains, With Special Emphasis on the Limpopo Complex of Southern Africa*, edited by D. D. van Reenen, J. Kramers, S. McCourt, and L. L. Perchuk Geological Society of America Memoir 207, 1–11. https://doi.org/10.1130/2011.1207(09).

Vernon, R., and G. Clarke. 2008. *Principles of Metamorphic Petrology*. Cambridge University Press.

Vernon, R. H., and S. E. Johnson. 2000. "Transition From Gneiss to Migma-tite and the Relationship of Leucosome to Peraluminous Granite in the Cooma Complex, SE Australia. In: Jessell M. W. & Urai J. L. eds. Stress, Strain and Structure. A Volume in Honour of W. D. Means." *Journal of the Virtual Explorer* 2. https://www.virtualexplorer.com.au/VEjournal/Volume2.

Villaros, A., S. Gary, M. Jean-Francois, and I. Buick. 2009. "The Trace Element Compositions of S-Type Granites: Evidence for Disequilibrium Melting and Accessory Phase Entrainment in the Source." *Contributions to Mineralogy and Petrology* 158, no. 4: 543–561.

Wang, W., E. Dunkley, G. L. Clarke, and N. R. Daczko. 2014. "The Evolution of Zircon During Low-P Partial Melting of Metapelitic Rocks: Theoretical Predictions and a Case Study from Mt Stafford, Central Australia." *Journal of Metamorphic Geology* 32, no. 8: 791–808.

Wendlandt, R., and W. Harrison. 1979. "Rare Earth Partitioning Between Immiscible Carbonate and Silicate Liquids and CO_2 Vapor: Results and Implications for the Formation of Light Rare Earth-Enriched Rocks." *Contributions to Mineralogy and Petrology* 409-419: 409–419.

White, R., R. Powell, and T. Holland. 2001. "Calculation of Partial Melting Equilibria in the System Na_2O–CaO–K_2O–FeO–MgO–Al_2O_3–SiO_2–H_2O (NCKFMASH)." *Journal of Metamorphic Geology* 19, no. 2: 139–153.

Whitney, D., and B. Evans. 2010. "Abbreviations for the Names of Rock-Forming Minerals." *American Mineralogist* 95: 185–187.

Wintsch, R., and J. Dunning. 1985. "The Effect of Dislocation Density on the Aqueous Solubility of Quartz and Some Geologic Implications: A Theoretical Approach." *Journal of Geophysical Research* 90, no. B5: 3649–3657.

Wintsch, R., R. Christoffersen, and A. Kronenberg. 1995. "Fluid-Rock Reaction Weakening of Fault Zones." *Journal of Geophysical Research* 100, no. B7: 13021–13032.

Yardley, B. 2005. "Metal Concentrations in Crustal Fluids and Their Relationship to Ore Formation." *Economic Geology* 100, no. 4: 613–632.

Yardley, B. W. 2009. "The Role of Water in the Evolution of the Continental Crust." *Journal of the Geological Society* 166, no. 4: 585–600.

Yardley, B. W., and R. J. Bodnar. 2014. "Fluids in Continental Crust." *Geochemical Perspectives* 3, no. 1: 1–2.

Yardley, B., S. Gleeson, S. Bruce, and D. Banks. 2000. "Origin of Retrograde Fluids in Metamorphic Rocks." *Journal of Geochemical Exploration* 69: 281–285.

Supporting Information

Additional supporting information can be found online in the Supporting Information section. **Figure S1:** Stacked area graph of the variation of modal mineralogy across samples. **Table S1:** Concentrations (parts per million—ppm) of standards in LA-ICP–MS. **Table S2:** 1 sigma error of the samples analysed in LA-ICP–MS. **Figure S2:** TiO_2/Al_2O_3 vs. FeO/Al_2O_3 plot. **Figure S3:** Gresens' type plot has been presented for each of the 4 transects where concentration of the major and rare earth elements of the high strain sample has been plotted against that of the low strain sample. In each of the plots, the elements in squared brackets have been chosen to draw the isochon lines. The justification of the choice of different elements in each scenario has been discussed in the text.